ABSTRACT

Title of Thesis: CRYOGENIC ATOMIC FORCE MICROSCOPE FOR CHARACTERIZATION OF NANOSTRUCTURES

Changyi Li, Master of Science, 2005

Thesis directed by: Professor Chia-Hung Yang
Department of Electrical and Computer Engineering

In this thesis, we present the design and applications of a cryogenic atomic force microscope (AFM) for characterization of nanostructures. The cryogenic AFM with a conductive tip can measure DC current through nanostructures. We use quartz tuning fork (QTF) as the force sensor. Unique coarse z motor design provides reliable autoapporach in the Z direction. AFM imaging with 10nm horizontal and ~2Å vertical resolution has been achieved. We have used this AFM in the current-voltage characterization of diodes, and, with a modified sensing mechanism, electrical force microscopy (EFM) and magnetic force microscopy (MFM) have been demonstrated.

CRYOGENIC ATOMIC FORCE MICROSCOPE

FOR CHARACTERIZATION OF NANOSTRUCTURES

By

Changyi Li

Thesis submitted to the Faculty of the Graduate School of the
University of Maryland, College Park, in partial fulfillment
of the requirements for the degree of
Master of Science
2005

Advisory Committee:

Professor Chia-Hung Yang, Chair
Professor Ping-Tong Ho
Professor Martin Peckerar

ACKNOWLEDGEMENTS

I want to express my appreciation to my research advisor Professor C.H.Yang. Without his patience and helpful guidance, it is impossible for me to finish this thesis.

I particularly owe my thanks to Dr. M. J. Yang for the MBE samples, to my colleagues G. M. Jones and Arun S Mampazhy for the sample preparation, to Mr. John Pyle for his help in the machine shop and to all of various others who helped me on different occasions.

I would like to thank my wife and all of my family for their unlimited supports and encouragements during my years of study.

Finally I thank the Department of Electrical and Computer Engineering, and the University of Maryland at College Park for an excellent study environment.

TABLE OF CONTENTS

TABLE OF CONTENTS…… iii

Chapter 1 Introduction…… 1

1.1 Scanning Probe Microscopy……. 1

1.2 Challenges in AFM……... 2

1.2.1 Nonmonotonic force curve……..……. 2

1.2.2 Instability - jump to contact……. 3

1.2.3 Contribution of other long-range forces……... 4

1.3 Force sensor…….. 4

1.4 Operating modes of AFM……. 5

1.4.1 Static AFM……... 5

1.4.2 Dynamic AFM……. 6

1.5 Noise in frequency modulation AFM……... 8

1.5.1 Generic calculation…….. 8

1.5.2 Noise in frequency measurement……. 9

1.5.3 Optimal amplitude for minimal vertical noise……. 10

Chapter 2 System design……. 11

2.1 System diagram……. 11

2.2 AFM head……. 12

2.3 Coarse z motor…….. 13

2.4 Piezo tube scanners……... 18

2.5 Pt/Ir Tip etching…… 19

2.6 Ni tip etching……. 23

2.7 Tip mounting……. 24

Chapter 3 System performance analysis……. 26

3.1 System circuit diagram…….. 26

3.2 Transimpedance amplifier……. 26

3.3 Quartz Tuning Fork force sensor…….. 28

3.4 Noise analysis……... 31

Chapter 4 Experiments…… 35

4.1 Resonant Interband Tunneling Diode (RITD)…….. 35

4.2 EFM…….. 42

4.3 MFM……. 45

Chapter 5 Conclusion…….. 49

Appendix A: Tip′s equation of motion……... 50

Appendix B: Circuit diagrams of coarse z motor driving boards……... 53

(a). Small signal board…… 53

(b). Large signal board…… 54

REFERENCE…….. 55

Chapter 1 Introduction

1.1 Scanning Probe Microscopy

Imaging individual atoms on a solid surface was impossible until the introduction of the scanning tunneling microscope (STM) in 1981 by Binnig, Rohrer, Gerber and Weibel.[1] In 1983, the adatom layer of Si(111)-(7×7) was imaged with an STM.[2] G.Binnig and Hrohrer were rewarded with the Nobel Prize in the Physics in 1986. After the invention of the STM, a large number of metals and semiconductors had been investigated on the atomic scale. Today, the STM is widely used in many areas, such as surface science, superconductivity, biochemistry and semiconductor physics etc.[2-4] The principle of STM is well explained in many books and review articles.[7-13]

Despite the success of the STM, it has a limitation. Because it uses the tunneling current between a biased tip and a sample as the feedback signal, it requires that the sample material must be electrically conductive. And even conductors (conductive metals and semiconductors) cannot be studied in ambient conditions by STM except for a few special materials, like highly oriented pyrolytic graphite (HOPG). Instead they have to be investigated in an ultrahigh vacuum because the surface layer of solids constantly changes by adsorption and desorption of atoms and molecules in ambient conditions.

Early STM experiments showed that when the tip-sample distance was small enough that a current could flow, significant forces would act with the tunneling current.[14] Based on the effect, in 1986, Binnig [15] invented the atomic force microscope.

It took five years before atomic resolution on inert surfaces could be demonstrated,[16, 17] and resolving reactive surfaces by AFM with atomic resolution took almost a decade from the invention of the AFM. The Si(111)-(7×7) surface was resolved with atomic resolution by dynamic atomic force microscopy by Giessibl in 1995.[18] The invention of frequency modulation techniques[19, 20] further improved the resolution and the scan speed of AFM.

Because electrical conductivity of the sample is irrelevant in AFM, the AFM can image virtually any flat solid surfaces without the need for surface preparation. However an ultrahigh-vacuum environment is required for studying most surfaces on the atomic level.

In addition, related microcopies based on AFM, such as electric force microscopy (EFM), magnetic force microscopy (MFM),[6,21,22] lateral force microscopy (LFM),[25] phase contrast imaging,[31] scanning conductance microscopy (SCM)[43] and scanning near field optical microscopy (SNOM)[29] have been developed.

1.2 Challenges in AFM [5]

AFM is closely related to the STM, and they share key components except for the probe tips. However AFM have more challenges with respect to STM.

1.2.1 Nonmonotonic force curve

For STM, the magnitude of the tunneling current increases monotonically as the tip-sample distance decreases, i.e., the tunneling current increases exponentially. This property allows a simple implementation of a feedback loop: the tunneling current is fed into a logarithmic amplifier to produce an error signal that is linear to the tip-

sample distance. For AFM, however, the force between tip and sample is not monotonic as shown Fig.1.1. In general, the force is attractive for large distance, e.g. larger than 20nm, and the force turns repulsive when between tip and sample distance is small, e.g. less than 2nm. Stable feedback is only possible on one branch of the force curve, where it is monotonic. So it is more complicated to establish a z distance feedback loop for an AFM than for STM.

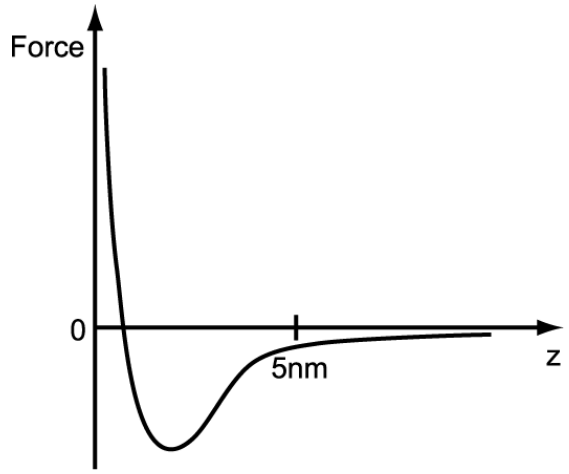

Fig.1.1 Typical nonmonotonic force curve in AFM

1.2.2 Instability- jump to contact

Because the tip is mounted on a spring, for instance a silicon cantilever, the tip could jump to and contact with the sample when the spring constant of the cantilever is less than a threshold value $k_{ts}^{\max}$, which is equal to $\max(-\partial^2 V_{ts}/\partial z^2)$.[23] Therefore, the tip cannot be approached to be very close to the sample. Of course the tip-sample distance cannot be well controlled under this condition. Jump-to-contact can be avoided even for soft cantilevers by oscillating the cantilever with a large enough amplitude A so that $kA > \max(-F_{ts}) = F_{ts}^{\max}$ [24] or using cantilevers with large spring

constants, or both. For our experiments, we choose QTF with high spring constant (~25000 N/m) to avoid this problem.

1.2.3 Contribution of other long-range forces

The force between the tip and the sample consists of long-range forces, such as electrostatic, magnetic and van der Waals, and short-range force, such as chemical force. In ambient condition there are also viscous forces. Equalizing the electrostatic potential between tip and sample can eliminate the electrostatic force. Using nonmagnetic tips can eliminate the magnetic force. The viscous force can be eliminated when the sample and tip are in vacuum. However, the van der Waals force cannot be switched off. For the dynamic AFM, will be covered in 1.4.2, The dependence of the frequency shift on amplitude shows that use of small amplitude helps to increase the sensitivity to short-range forces [26] because short-range forces have a very strong force gradient. While for large amplitudes, long-range forces contribute heavily to the frequency shift. [27,28].

1.3 Force sensor

For sensing normal tip-sample forces in AFM, the force sensor should be rigid in two axes and relatively soft in the third axis. This property is fulfilled with a cantilever beam. The first cantilevers were made from a gold foil with a small diamond tip attached to it.[15] Simple cantilevers could even be cut from household aluminum foil [42] and etched tungsten wires [22]. Later, silicon micro machining technology was employed to build cantilevers in parallel production with well-defined mechanical properties. The first micro machined cantilevers were built from SiO_2 and Si_3N_4 [22]. Later, cantilevers with integrated tips were machined from

silicon-on-insulator wafers.[44] The most common cantilevers in use today are built from all-silicon with integrated tips pointing in a [001] crystal direction. This method was developed by Wolter, Bayer, and Greschner [45] at IBM Sinderlfingen, Germany.

Around 1970, the watch industry was revolutionized with the introduction of quartz tuning forks as frequency standards in clocks. Experimental studies of using quartz based force sensors were carried out soon after the invention f the AFM. P.Güethner et al.[46] used tuning fork as force sensors in acoustic near-field microscopy, while Karrai and Grober [47] used a tuning fork to control the distance between the optical near-field probe and the surface in the scanning near field optical microscope. In comparison to the silicon cantilever, the QTF has high spring constant. And the most important advantage is its high Q factor which will increase scan speed and sensitivity when The QTF force sensor is used in the frequency modulation AFM.[34]

1.4 Operating modes of AFM

1.4.1 Static AFM

In the static atomic force microscopy, the force F_{ts} that acts between the tip and sample is used as the imaging signal. In the static mode of operation, the force is translated to the cantilever deflection by $d = F_{ts} / k$. Because the deflection of the cantilever should be significantly larger than the deformation of the tip and sample, restrictions on the useful range of k is apply. In the static mode, the cantilever should be much softer than the bonds between the bulk atoms in the tip and sample. Typical values for k in the static mode are 0.01-5 N/m. Inter-atomic force constants in solids are in a range from 10N/m to 100N/m, in biological samples, they can be as small as

0.1N/m. The eigenfrequency f_0 should be significantly higher than the desired detection bandwidth. For example, if ten lines per second are recorded during imaging a width of 100 atoms, f_0 should be at least $10\times2\times100\ s^{-1}$=2 kHz in order to prevent resonant excitation of the cantilever. Even though the static AFM has been demonstrated that atomic resolution is possible,[30] the method can only be applied in certain cases. The magnitude of $1/f$ noise can be reduced by low-temperature operation.[32] And the long-range attractive forces have to be canceled by immersing tip and sample in liquid [30] or by partly compensating for the attractive force by pulling at the cantilever after jump-to-contact has occurred.[32]

1.4.2 Dynamic AFM

There are two basic methods of dynamic operation: amplitude modulation (AM) and frequency modulation (FM) operation. In AM-AFM,[33] the actuator is driven by a fixed frequency f_{drive}, where f_{drive} is close to but different from f_0. When the tip approaches the sample, elastic and inelastic interactions cause a change in both the amplitude and the phase (relative to the driving signal) of the cantilever. Either change can be used as the feedback signal. The change in amplitude in AM mode does not occur instantaneously with a change in the tip-sample interaction, but on a time scale of $\tau_{AM} \approx 2Q/\omega_0$ (Please refer to the Appendix A for details). Therefore, for one example, for a high-Q cantilever in vacuum Q=50000 and a typical resonant frequency of 50kHz, the maximum available bandwidth is only 0.5Hz, which is too slow for most applications. It's therefore not practical to try to increase sensitivity by raising the Q to such high values.

Albrecht et al.[34] solved this problem by introducing the frequency-modulation (FM) mode. In the FM-AFM, a cantilever with eigenfrequency f_0 and spring constant k is subject to controlled positive feedback such that it oscillates with constant amplitude [20, 34] if the phase shift φ between the mechanical excitation generated at the actuator and the deflection of the cantilever is π/2. Most importantly, the change in the resonance frequency occurs within a single oscillation cycle on a time scale of $\tau_{FM} \approx 1/f_0$. Therefore compared with AM-AFM, the scan speed could be dramatically improved if the resonance frequency f_0 is very high. As we will see later, use high Q cantilever in vacuum will improve the resolution dramatically.[35, 36] FM-AFM has five parameters: the spring constant of the cantilever k, the eigenfrequency of the cantilever f_0, the quality factor value of the cantilever Q, the oscillation amplitude A and the frequency shift of the cantilever. The type of the cantilever determines the first three parameters and the last two parameters can be adjusted freely. Surprisingly, the amplitude necessary for obtaining good results were very large compared to atomic dimensions. The necessity of using large amplitudes for obtaining good images seems counterintuitive, because the tip of the cantilever spends only a small fraction of an oscillation cycle in the vicinity of the sample. Actually, the large amplitudes are required to prevent instabilities of the cantilever oscillation and reduce the noise in the feedback loop.

Our AFM is based on the frequency modulation, and the force sensor is quartz tuning fork because of its high Q factor and large spring constant. The reasons why we use QTF as the force sensor will be explained in the next section.

1.5 Noise in frequency modulation AFM [5]

1.5.1 Generic calculation

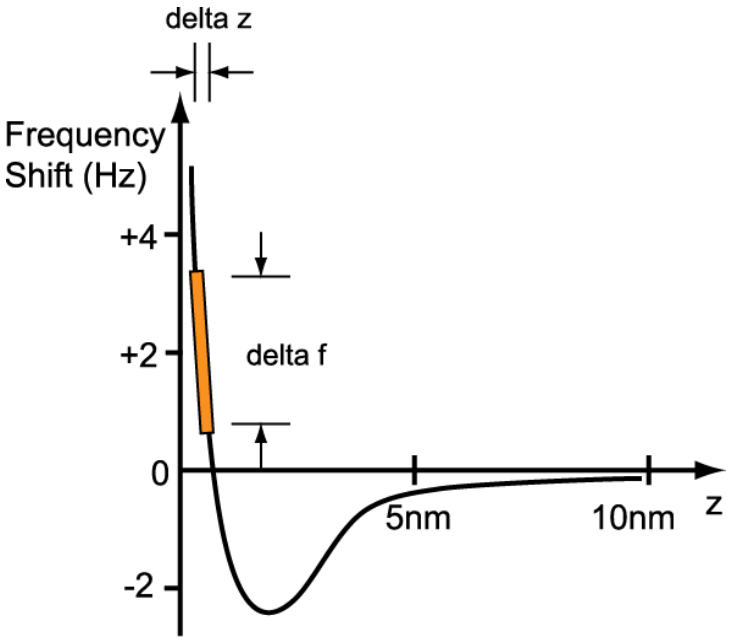

Fig. 1.2 Typical AFM approach curve measured at ambient condition.

Figure 1.2 is one typical AFM approach curve at ambient condition. The vertical noise in FM-AFM is given by the ratio between the noise in the imaging signal and the slope of the imaging signal with respect to z: $\delta z = \frac{\delta \Delta f}{\partial \Delta f / \partial z}$. Obviously low noise is obtained for a low-noise frequency measurement and a steep slope of the frequency-shift curve.

Additional boundary conditions need to be considered when we choose the operating point where the slope of the frequency-shift curve is appropriate. One boundary condition is that if we choose positive frequency shift as set point, the value shouldn't be too large. For our experiments, we find that 1 to 5 Hz is acceptable. This is because that if the force between front atom and the surface is too large, the front atom or larger sections of tip or sample can shear off. The second boundary condition

is that stable feedback of the microscope is only possible either on the branch of Δf with positive slope or on the one with negative slope because the frequency shift is not monotonic with respect to z. The Third boundary condition is that the frequency-versus-distance curve is a function of the lateral tip position. If the tip is directly over a sample atom, the minimum can be very sharp. However, at other sample sites there may be small negative frequency shift. Imaging can only be performed with frequency-shift set points that are reachable on every (x,y) position on the imaged sample area, otherwise a tip crash occurs.

1.5.2 Noise in frequency measurement

The vertical noise equation $\delta z = \frac{\delta \Delta f}{\partial \Delta f / \partial z}$ shows that the accuracy of the frequency-shift measurement determines directly the vertical resolution. Reduce the frequency noise is another big issue need to be addressed to achieve high resolution.

The frequency noise has two major contributors: thermal noise of the quartz tuning fork and frequency detector noise. Martin et al.[37] and McClelland et al.[22] studied the influence of thermal noise on the silicon cantilever and Albrecht et al.[34] and Smith[38] calculated the thermal limit of the frequency noise. They all come to a similar conclusion that the square of the relative frequency noise is given by the ratio between the thermal energy of the cantilever $k_B T$ and the mechanical energy stored in it $\frac{1}{2} kA^2$ divided by its quality factor Q and multiplied by the ratio between bandwidth B and cantilever eigenfrequency f_0. Specifically, Albrecht et al.[34] find that $\delta f_{thermal} = \sqrt{\frac{\omega_0}{2\pi} k_B T B / (\frac{1}{2} k A^2 Q)}$

The frequency detector noise is determined by the frequency demodulator. Giessibl [39] and Dürig et al.[40] find $\delta f_{\text{detector}} \propto B_{FM}^{3/2}$, where B_{FM} is the low-pass filter bandwidth in the phase-locked loop. For our easyPLL plus Digital FM-Detector made by Nanosurf, the best frequency resolution is 5mHz if the measurement range is in ±183Hz. Of course the input signal (amplitude, frequency et al.) and bandwidth in the phase-locked loop will change the frequency resolution value. For our case, B_{FM} is 400Hz. The noise in the two-stage transimpedance amplifier will increase the frequency detector noise of course because $\delta f = \sqrt{\delta f_{\text{detector}}^2 + \delta f_{thermal}^2}$. For most setups, thermal noise is negligible compared to detector noise.

1.5.3 Optimal amplitude for minimal vertical noise

From the above discussion, we know that both the nominator and denominator in $\delta z = \frac{\delta \Delta f}{\partial \Delta f / \partial z}$ are functions of the quartz tuning fork oscillation amplitude. Giessibl et al.[41] addressed this issue. They find that there is minimal noise for amplitudes on the order of the range of the tip sample force F_{ts}. For example, for the chemical forces, the range of F_{ts} is ~1Å. However, in our experiments, we find out that we need to choose the amplitude large enough to have strong enough signal to keep the feedback loop stable. One reason is that we want to get fast scan speed in a large scan area. While if we just focus on the ~Å resolution, the scan speed has to be too slow to be practical for scanning a large area.

Chapter 2 System design

2.1 System diagram

Our AFM system is designed for measuring characteristics of nanoscale structures at low temperature and under intense magnetic fields. Fig. 2.1 is the schematic of our AFM system.

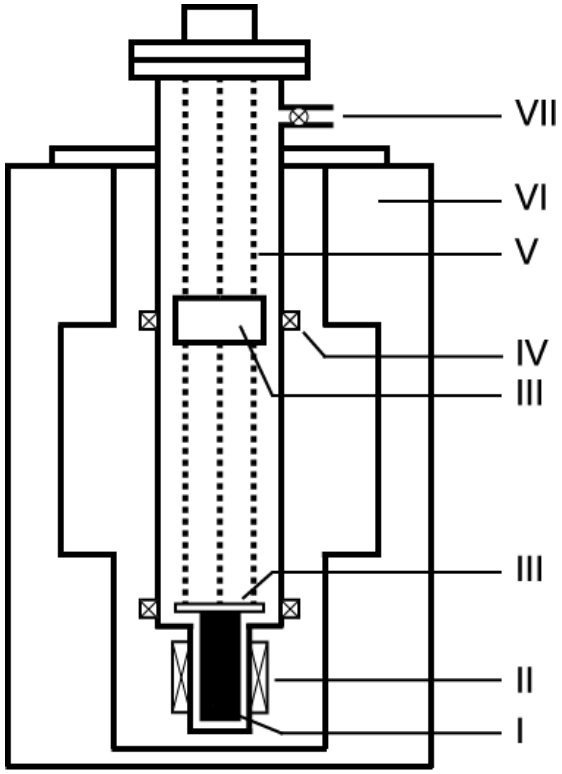

Fig. 2.1 Schematic of the AFM system (not in scale): (I) AFM head, (II) Superconducting magnet, (III) copper blocks, (IV) Neodymium-Iron-Boron magnets, (V) spring, (VI) experiment dewar, and (VII) pumping port.

The AFM head is so small that it can fit into a bore (38mm) of a superconducting magnet. The AFM head is attached to a copper plate, which is suspended by three springs. The spring constant is 18 kg/m. Three Neodymium-Iron-Boron magnets (0.3 Tesla, rectangular, 12.7mm×12.7mm×6.35mm) are used to damp

the spring/copper plate/AFM head by eddy current. The second damping stage is built in the same way.[48] The springs/copper plates/AFM head is enclosed in a vacuum chamber, which is mounted on an optical table. The table can be floated in order to further reduce the vibration coupling during scanning.

2.2 AFM head

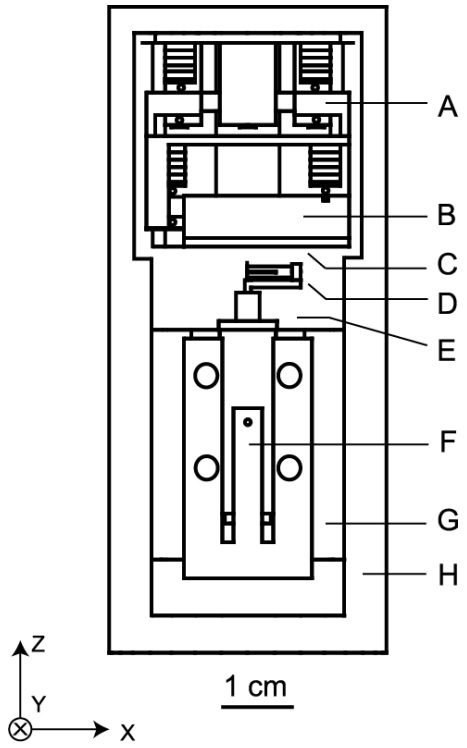

Fig. 2.2 Schematic of AFM head: (A) coarse x stage. (B) coarse y stage. (C) sample holder. (D) QTF with tip. (E) double-tube scanner. (F) copper-beryllium leaf spring. (G) Hexagonal piezo stack housing for coarse z motor. (H) AFM stainless steel housing.

Figure 2.2 is the schematic of our AFM head design. The AFM head consists of coarse x stage, coarse y stage, coarse z stage, sample holder, double-tube scanner and the stainless steel housing. The coarse x/y stage and coarse z stage are fit into a

1.25” ID stainless steel tube. Initial principal [49-51] based coarse x/y stages have the movement range ±2 mm in x direction, ±2.5 mm in y direction.

2.3 Coarse z motor

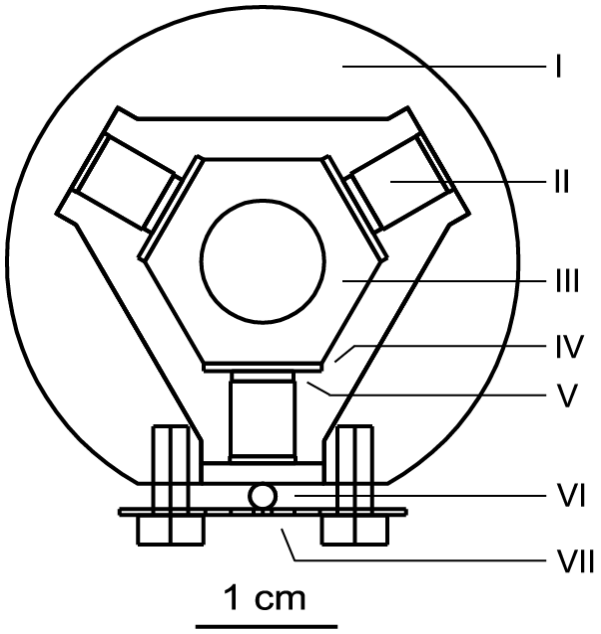

Fig. 2.3 Schematics of coarse z motor: (I) Hexagonal piezo stack housing. (II) 4-layer shear mode piezo stack. (III) inner macor tube (movable part). (IV) sapphire plate. (V) Alumina plate. (VI) sapphire ball. (VII) copper-beryllium leaf spring.

Coarse Z design is very important in the cryogenic scanning probe systems because the tip need to be driven by the coarse z motor to approach to the sample close enough. For our design, less than 1μm is necessary which is the half of our Z scanner’s full range. Therefore the reliability for the motor to work at both room temperature and low temperature is very critical.

Figure 2.3 shows the schematic of our coarse z motor. Three sapphire plates are glued on the hexagonal macor tube. The macor with sapphire plates together are hold by equally distributed piezo stacks. Each piezo stack consists of four

4mm×4mm×1mm EBL #2 shear mode piezo slabs. To avoid arcing, small parts of the electrodes are milled out along the edges of the piezo slabs. These four piezo slabs are glued together using conductive epoxy and little non-conductive epoxy is applied onto the edges of the piezo slabs. One alumina plate is glued on the top of each stack, and the alumina plates will directly contact with the sapphire plate on the macor tube. The hexagonal titanium housing is machined by EDM. Four piezo stacks are glued onto the housing by non-conductive epoxy. The other two piezo stacks on the front side are glued on one macor rectangle. One sapphire ball is glued on the outside of the macor rectangle. One special designed leaf spring is used to push the sapphire ball. We find out that choose the appropriate number of the leaf spring, the pushing force can be tuned very well. The design of the leaf spring has large enough tolerance to handle thermal shrinkage during cooling procedure. In this design, the forces applied on the six piezo-stacks are equal and the force change will be negligible at different temperature.

The operation principle of our coarse z motor is similar to Pan's design.[54, 55] A homebuilt large signal board and a small signal board generate the driving signals shown in Fig. 2.4. Please refer to the Appendix B for the circuit diagrams of the two driving boards. In Fig. 2.4, those 0.1ms delayed 6 channel signals will be used to drive the six shear mode piezo stacks one by one. When one stack deforms, the other 5 stacks do not deform, and the 5 stacks can hold the hexagonal macor without movement. After 0.5ms, all 6 stacks deform but the hexagonal macor still haven't moved yet. Then same signals are applied to the six stacks. These stacks will deform back to there normal position. The hexagonal will move now because all six stacks

deform at the same time. These steps repeat and the hexagonal macor will move linearly toward one direction. The x/y/z piezo scanner is glued into the macor tube. Therefore, the tip can approach to or retract from the sample. (If the sign of driving signals are reversed, the hexagonal macor will move in an opposite direction.)

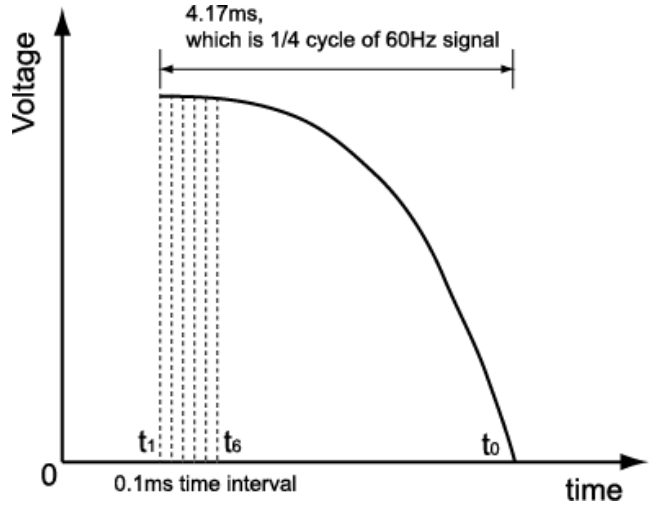

Fig. 2.4 Schematics of six-channel driving signals for the coarse z motor.

The full travel distance of the motor is about 1cm, which is limited by the length of the housing and hexagonal macor. It can be longer than 1cm but for our purpose 1cm is long enough. The coarse z motor is tested at room temperature, 77K, and 4.2K by measuring capacitance. One electrode of the capacitor is fixed on the motor housing and another electrode is fixed on the hexagonal macor that is the movable part. Therefore by measuring the capacitance, the relative position of the hexagonal macor and the motor housing can be detected. The capacitance is measured by Keithley 590 CV analyzer at 100KHz. Fig. 2.5, Fig. 2.6 and Fig. 2.7 show the capacitance measured at 300K, 77K and 4.2K respectively.

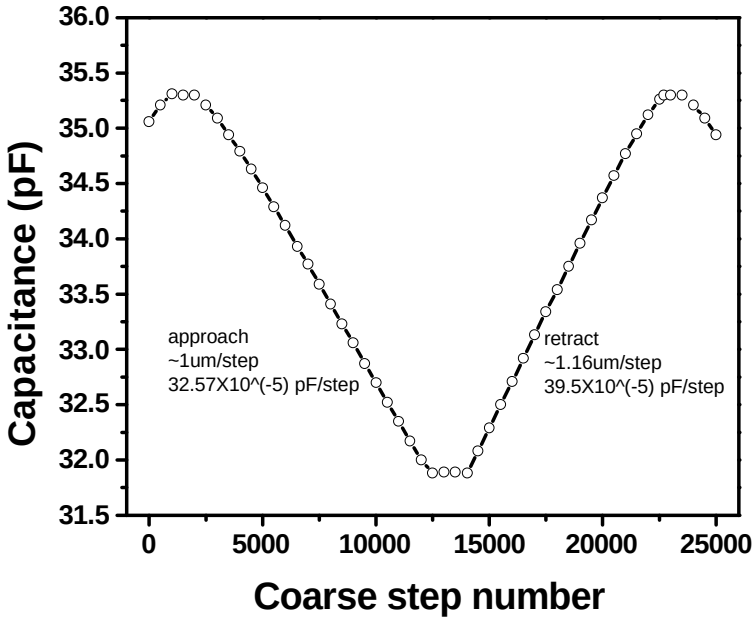

Fig.2.5 Capacitance measurements when the coarse z motor is working at 300 Kelvin.

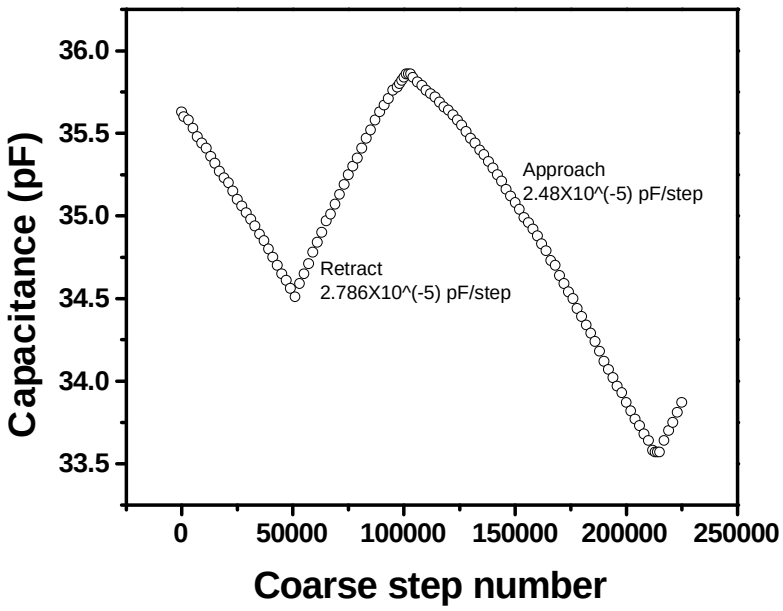

Fig. 2.6 Capacitance measurements when the coarse z motor is working at 77 Kelvin.

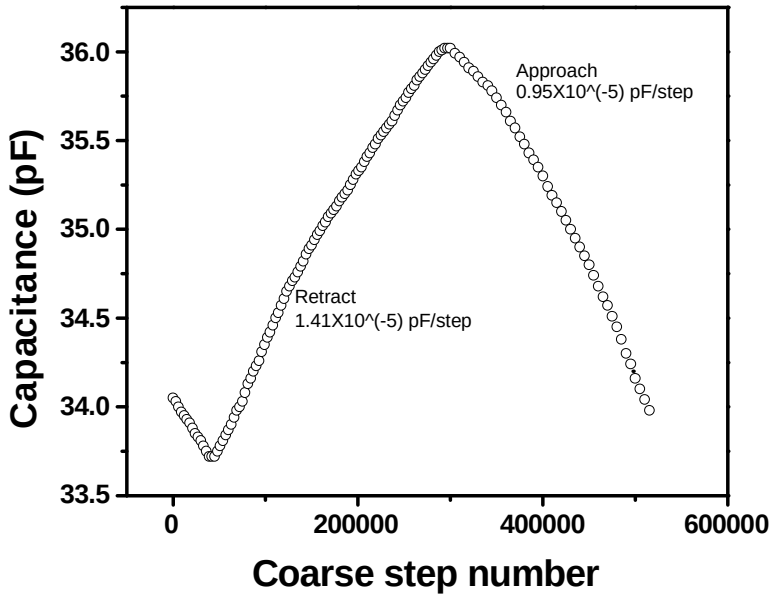

Fig. 2.7 Capacitance measurements when the coarse z motor is working at 4.2 Kelvin.

The absolute capacitance value doesn't mean too much because the wire distribution could change the absolute capacitance value. Therefore, we only care about the relative capacitance change when the coarse z motor is working.

By comparing the measured data, we find out that the step sizes are very different at different temperature. The step size ratio is 41.5: 2.6: 1 at 300k, 77k and 4.2k. The ratio is much larger than the calculated value 5.5:1 at 300K and 4.2K. (The piezo coefficient d_{31} at 300k and at 4.2k has the ratio of 5.5:1.) The possible reason is that at lower temperature, the strain value of the piezo slabs is lower. Then it will be harder for the piezo stack to overcome the resistance caused by the friction between the alumina plate and the sapphire plate or caused by the nonconductive epoxy around the piezo stacks. Even though the step size reduces much more than what we

expect, the motor is still working. And also the linearity of movement is good. This is very encouraging because this linear motor could be used at cryogenic condition under very precise control.

2.4 Piezo tube scanners

To have the ability for our system to scan large area, we choose 1-inch long piezo ceramic tubes as our x/y and z scanner.

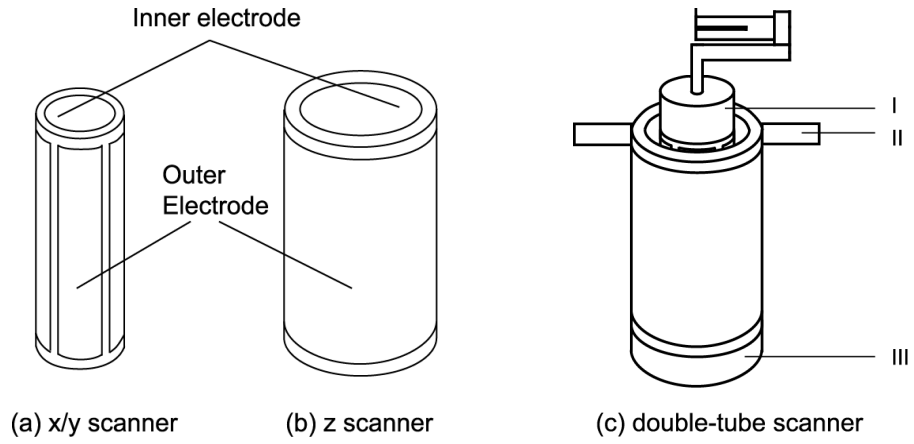

Fig. 2.8 Schematics of x/y and z scanners. (a) and (b) are x/y and z piezo ceramic tube scanners. (c) is the schematics of the assembly of the x/y/z scanner. (I) is a macor spacer. (II) is the macor seat to fix the z scanner onto the coarse z motor. (III) macor seat to fix x/y scanner and z scanner together.

Figure 2.8(a) is piezo ceramic tube for the x/y scan. The tube has 0.125” OD with equally separated quadrants, 0.12”OD, 0.02” wall thickness, 1” long and also 0.05” electrode is removed on OD at both ends. Fig. 2.8(b) is the z scanner that is 1” long, and has 0.25” OD, 0.02” wall thickness. And also 0.05” electrode is removal at both ends. The OD electrode of the z scanner is polarized “+”. When OD electrode is biased positively relative to ID electrode, the z tube will retract. Our double-tube

design minimizes the thermal expansion problem caused by very long scanning tubes. We fix one end of x/y tube and one end of z tube together at Fig.2.8(c) III, and the other end of z tube is fixed to the coarse z motor at Fig.2.8(c) II. Because of this design, the thermal expansion could be canceled, and then the thermal expansion caused distortion at tip end could be negligible. Based on the parameters of the piezo ceramic tubes that d_{31}= -1.73Å/V at room temperature, and –0.31 Å/V at 4.2Kelvin. We calculate the conversion ratio of the z piezo tube as at room temperature is 77.85 Å/V, and at 4.2Kelvin, the conversion ratio is 13.95 Å/V. For the X/Y scanner we get the conversion ratio for X/Y scanner as 158nm/V at room temperature and 32nm/V at 4.2K. Those conversion ratio numbers will be used as parameters in the control unit, which will generate appropriate signals to drive those tubes during scanning.

2.5 Pt/Ir Tip etching

Our Pt/Ir tip etching procedure is based on J. Lindahl et al's paper.[56] And the material is 3mil diameter Pt_{90}/Ir_{10} wire. The following is the procedure for the tip etching. To get very sharp tip (curvature ~20nm) all of the three steps are needed, and especially step 1a is very critical. To get not very sharp tip (for example, curvature > 500nm) only step 1b and step 3 are necessary.

Step 1: We use saturated $NaCl/H_2O$ solution as the etchant. As we can see in Fig.2.9, The 3mil diameter Pt_{90}/Ir_{10} wire is hold by a metal clip that is used as one electrode. One graphite rod is used as another electrode that is dipped into the etchant. The Pt_{90}/Ir_{10} wire is lowered by a micromanipulator into the etchant about 2mm deep. 20Vrms AC voltage source is applied onto the metal clip. The etching current is

monitored using a current meter. Depends on how sharp tip we want to make, we should control the tip shape in this step by controlling the cutoff current.

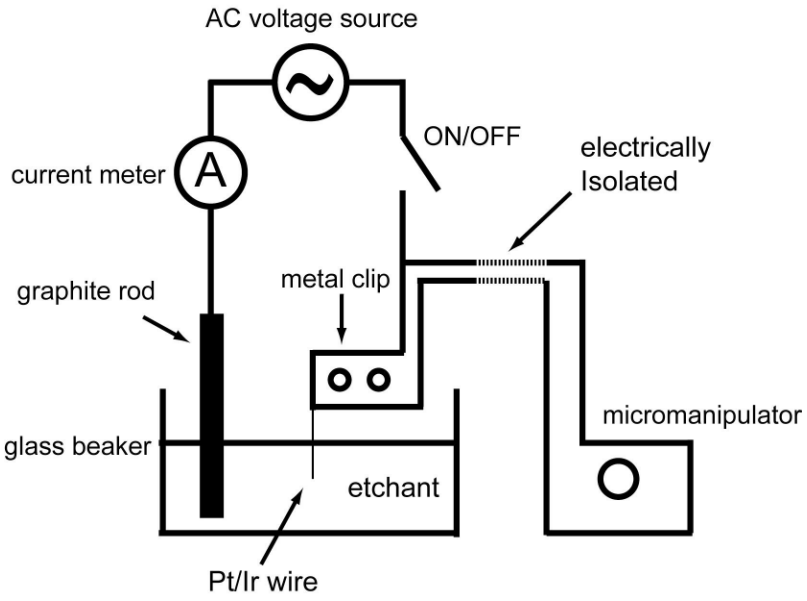

Fig. 2.9 Schematics of tip etching setup.

a). If we want to get the best resolution, the tip must be as sharp as possible. In this case, we should get the droplet shaped tip in this step 1, as shown in Fig.2.10, then the tip will be further polished in step 2 to get the very sharp tip (~30nm). To get the droplet shaped tip, etching must be stopped when the etching current reaches ¼ of the original etching current. The current drop is not very fast. It will take several minutes. Based on my experience, no additional control electronics are necessary to turn the etching bias off automatically. One can turn off the etching current by hand when the current reaches about ¼ of the original etching current. Less than 5 seconds turn-off time error is acceptable.

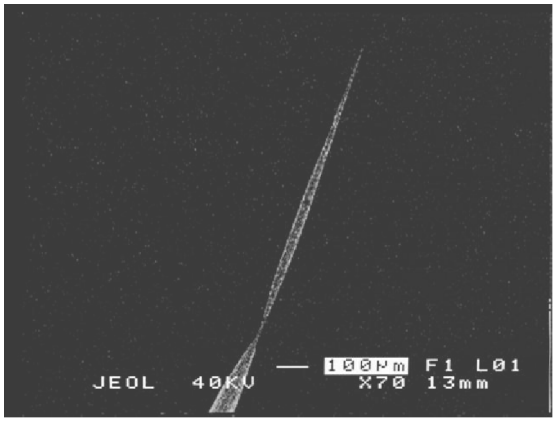

Fig. 2.10 Typical droplet shaped tip

b). If we want to do the direct contact measurements where the tip will be used to physically touch the sample. To avoid the easy damage of the tip, tip with relatively larger curvature is required. To get the the tip with about 200nm or larger curvature, the etching time must be long enough to avoid the droplet shape. After we see the droplet part drops off, wait for another 10s seconds, and we can get the tip with ~200nm curvature routinely. (Based on my experience, the whole process will last about 5 minutes from the beginning of etching) Longer etching time, larger tip curvature will be achieved. Using this method, we can get tips with ~500nm curvature easily as shown in Fig. 2.11.

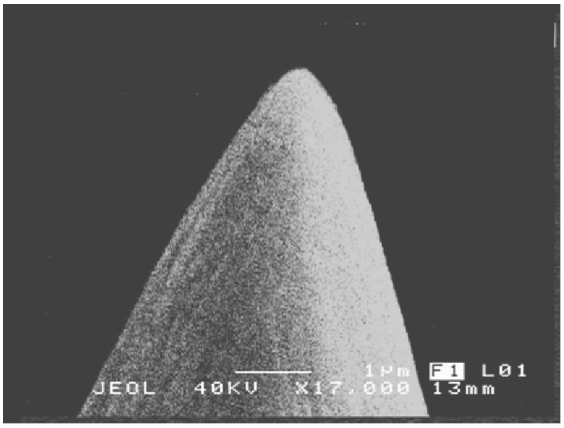

Fig. 2.11 SEM image of a typical tip for direct contact measurement

Step 2: H_2SO_4 Polish to get very sharp tip. In this step we will use tips with droplets (made in step 1a) to get very sharp tips. The etchant is H_2SO_4 : H_2O=2:1(Volume ratio) now, and the 4 KHz square wave is applied onto the droplet shaped tip through the metal clip. The details on the 4KHz square wave are: +10V for 40μs and -0.5V for 210 μs. After about 2-6 minutes (time depends on the waist thickness of the droplet shaped tip gotten in step 1a) the droplet part of the tip will drop off (A simple telescope is very helpful in this step). Then one should wait for additional several 10s seconds (for example 30seconds) to get smoother shape. Fig.2.12 shows the SEM images of a typical sharp tip with ~30nm curvature.

Fig. 2.12 SEM images of a typical sharp tip with ~30nm curvature

Step 3: Deoxidation. Deoxidation is necessary for both very sharp tip and not very sharp tip for direct contact measurements, even though the oxidation for Pt/Ir tip is relatively weak compared with W tip. To deoxidize the tip, we should carefully dip the tip into HCl:H_2O=2:1 (volume ratio) and wait for about 30 seconds. Then carefully pull the tip out and put it on one tip holder. In this step the chemical reaction equation is PtO_2+6HCl=H_2PtCl_6+2H_2O. This step is required for the direct contact measurements to make sure good Ohmic contact. Based on our direct contact experiments with gold film, the minimum contact resistance we got was 33ohm.

2.6 Ni tip etching [57]

Procedure: Start with 250um-diam wire and electrochemically etch one end in a solution of 20% HCl. During etching, a 60-Hz ac voltage of 1.5rms is applied between the wire and a graphite electrode. The wire is immersed about 5mm into the solution and etching is allowed to continue until the wire begins to perceptibly shorten (Usually about 4min).

The resulting etched wire should have a sharp point and a narrow taper angle. Putting more or less of the wire into the solution initially can alter the taper angle. The HCl concentration and AC voltage may also be varied to alter tip shape. I will usually stop etching when the etching current is about 45mA and can get tips with about 300nm curvature. To get sharper tip, etching should be stopped when the etching current is about 50mA. To get tip with large curvature (say >500nm), etching should be stopped at about 40mA. Fig. 2.13 are SEM images of electrochemically etched Ni tips. These numbers are experimental data for our specific setup, and they could be changed for desired tip shapes.

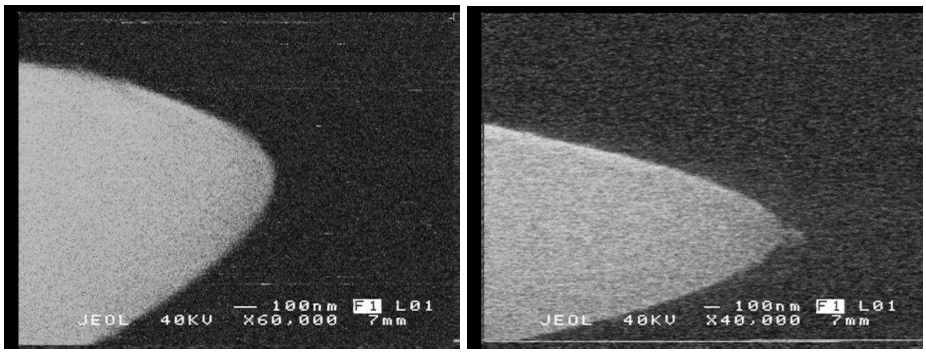

Fig. 2.13 SEM images of electrochemically etched Ni tips. (a) and (b) are SEM images of tips with different curvatures.

2.7 Tip mounting

Tip mounting is very critical to get high enough Q factor of the QTF force sensor so that the system sensitivity can be improved because of high Q factor.[34] After long time testing, we find out that the method with following steps are very effective, and the Q factor after all those steps could reach ~8000 which is high enough for our FM-AFM to get high resolution.

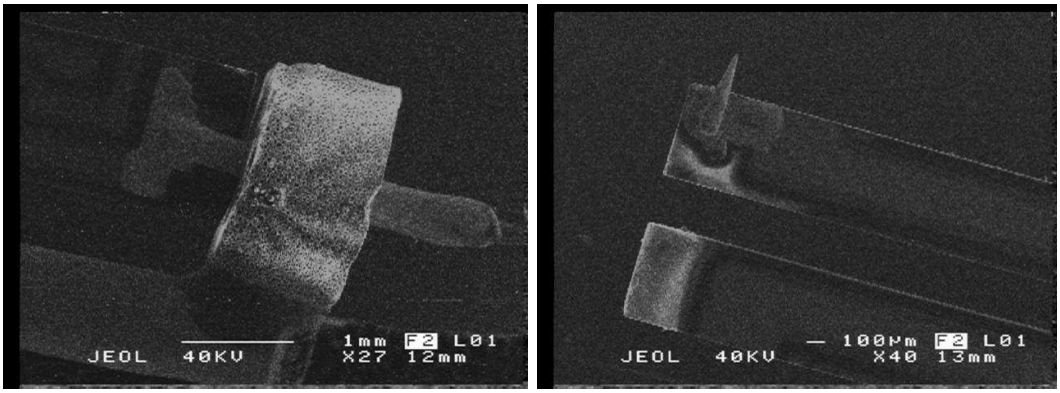

Fig. 2.14 SEM images of mounted QTF with a tip

The following eight steps are the details of tip mounting. 1). Carefully break vacuum seal of the commercial QTF which is ECS 3x8 model. 2). Glue the glass base of the QTF on a 1mm diameter L-shape stainless steel rod with non-conductive epoxy (H77). The stainless steel rod is bended to "L" shape so when stainless steel rod is mounted onto the scanner, this tip can be close enough to the center of the sample holder. Put one drop of non-conductive epoxy at the corner of the "L" shaped stainless steel rod. This drop of epoxy will be used as one fixed point for the gold wire in step 7 if necessary. Bake in oven for 1 hour at 150^{o}C. See Fig.3.3 (a) for the "L" shape stainless steel and QTF with tip. 3). After baking, measure the impedance of the baked QTF to make sure its Q is high enough (~15000). 4). Put one very tiny drop of conductive epoxy (H21D) on the end of the one prong of the QTF. Hold the

etched tip end with a sharp tweezers. (The tweezers should hold the Pt/Ir wire where is very close to the tip but must be very careful that the tip should not be damaged.) Cut the Pt/Ir wire close to the tweezers. (As you can see from the SEM image, we can cut the tip as short as about 1mm). Carefully put the tip onto the conductive epoxy and align the tip well. Bake in oven for 30 minutes at 120^{o}C. 5). After baking, measure the impedance of the QTF to make sure its Q is not smaller than 10000. 6). Cut the two leads of the QTF to be about 1mm long, and solder thin wires (45 Heavy formvar from MWS) on the two leads for electrically driving the QTF. 7). Put very tiny drop of conductive epoxy (H21D) on cut end of the tip and also put one small drop of the conductive epoxy on the non-conductive epoxy (prepared in step 1) at the corner of stainless steel rod. Put 1mil gold wire into the two drops of epoxy. Make sure the gold wire is loose enough between these two points covered by conductive epoxy, and it's long enough after the stainless steel rod). Bake at oven for 30 minutes at 120^{o}C. 8). After baking, measure the Q of the QTF. Use a small tweezers to very carefully bend the gold wire between the two fixed epoxy points till the highest Q (~8000) is achieved.

All the steps are done with the help of a homemade QTF holder and under 40X optical microscope. Typically, Q changes to be around 8000 after all the 8 steps. And its resonance frequency changes from 32768Hz to be around 32KHz.

Chapter 3 System performance analysis

3.1 System circuit diagram

The circuit diagram of our whole system is show in Fig.3.1. Positive feedback control will make sure the QTF always oscillates at its resonance frequency. The force between tip and sample will change the resonance frequency of the QTF. The resonance frequency shift can be detected by easyPLL. The output voltage signal, which is proportional to the QTF resonance frequency shift, is fed into the control unit RHK. RHK will generate control signal to the XYZ scanner to approach tip to or retract tip from the sample based on the frequency shift signal detected by easyPLL. Therefore the tip-to-sample distance will be kept as a constant during scanning.

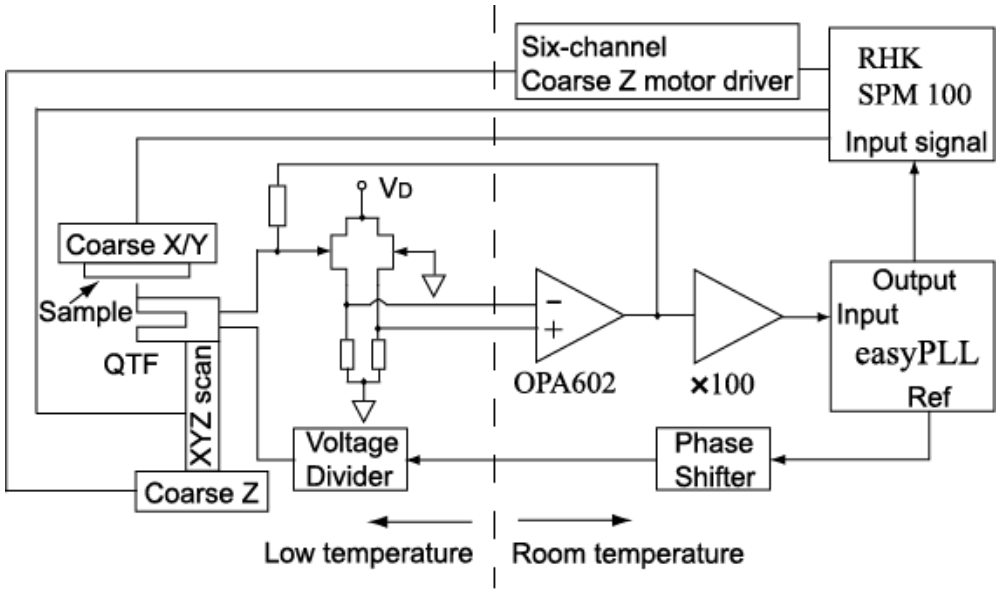

Fig. 3.1 System circuit block diagram

3.2 Transimpedance amplifier

Our transimpedance amplifier consists of two stages. The first stage is a source follower, which provides low output impedance, high input impedance, and a wide bandwidth. The characteristic low output impedance is useful in driving a 50 V

coaxial cable. The second stage is a low noise, wide band operational amplifier with a large voltage gain. A resistor R_f completes the feedback loop. Similar two-stage transimpedance amplifiers had been used for high impedance infrared detector amplifier at lower frequencies.[58] Yang et al.[60] explained the principle of global feedback.

The source follower uses two GaAs metal–Semiconductor field effect transistor (MESFET). We measure the characteristics of each MESFET at both room temperature and 4.2K, and write a program to compare them and choose two best-matched FETs to build the pair.

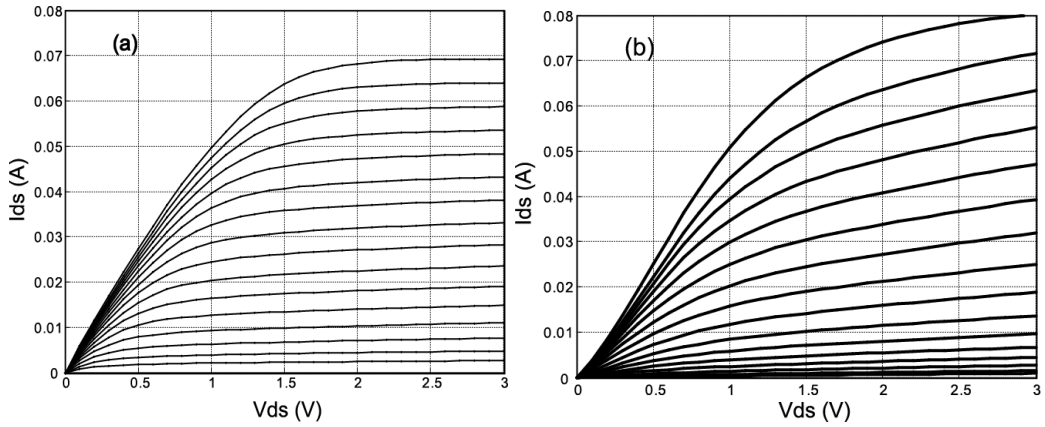

Fig. 3.2 MESFET characteristics in the common source configuration at (a) 300 K and (b) 4.2 K. Drain current is shown as a function of a sweeping drain bias and the gate bias is ranged from 0 (fully on, high drain current) to –1.5 V (close to zero drain current), with -0.1 V per step. The transistor, 3SK188, is a depletion mode, n-channel GaAs MESFET.

Figure 3.2(a) and Fig. 3.2(b) show the typical current-voltage characteristics of the MESFET at room temperature and at 4.2 K, respectively. In comparison with its room temperature characteristics, the current-voltage relation at 4.2K becomes

more nonlinear, and the transconductance decreases. The DC bias point of the source follower can be accurately determined once the source resistance and V_D are given. Feedback through R_f will guarantee that the dc offset at OPA602 output is close to zero. In practical, little OPA602 offset tune up is needed because the two MESFETs couldn't match perfectly. Because of its less-than-unity voltage gain, the bandwidth of the source follower is extended to the cutoff frequency f_0 the transistor. We use an OPA602 operational amplifier as the second stage, for it offers a reasonably high gain-bandwidth product and low noise. Because of the use of feedback and the high gain of OPA602, The nonlinearity and less-than-unity voltage gain of the first MESFET stage are unimportant. We chose a 1M-ohm metal film resistor and a paralleled 2pF capacitor as feedback components and got appropriate signal amplitude and signal to noise ratio.

3.3 Quartz Tuning Fork force sensor

The great benefit of the fork geometry is the high Q factor, which is a consequence of the presence of the oscillation mode in which both prongs oscillate opposite to each other. The dynamic forces necessary to keep the two prongs oscillation cancel in the case exactly. However, this only works if the eigenfrequency of both prongs matches precisely.

We tested the electrical properties of quartz tuning forks by measuring their impedance. As you can see in the Fig.3.3(c), the commercial QTF in can has a 2^{15}Hz resonance frequency and its impedance at resonance is about 17kΩ. The quality factor is about 55000. Once the vacuum can is broken, its resonance frequency changes to be 32757Hz. And its impedance at this resonance frequency is about

91kΩ. The quality factor is about 12000. When the tiny tip is glued on one prong of the tuning fork, its resonance frequency changes to be 32431Hz, and its impedance is about 114kΩ. The quality factor is about 10000. When the temperature goes to 4.2K, their quality factor will increase about 10times while their resonance frequencies reduce about several tens Hz. In the Fig.3.3 (d) we can also see the phase difference for the three cases: QTF in can, QTF in air and QTF in air but with tip glued on.

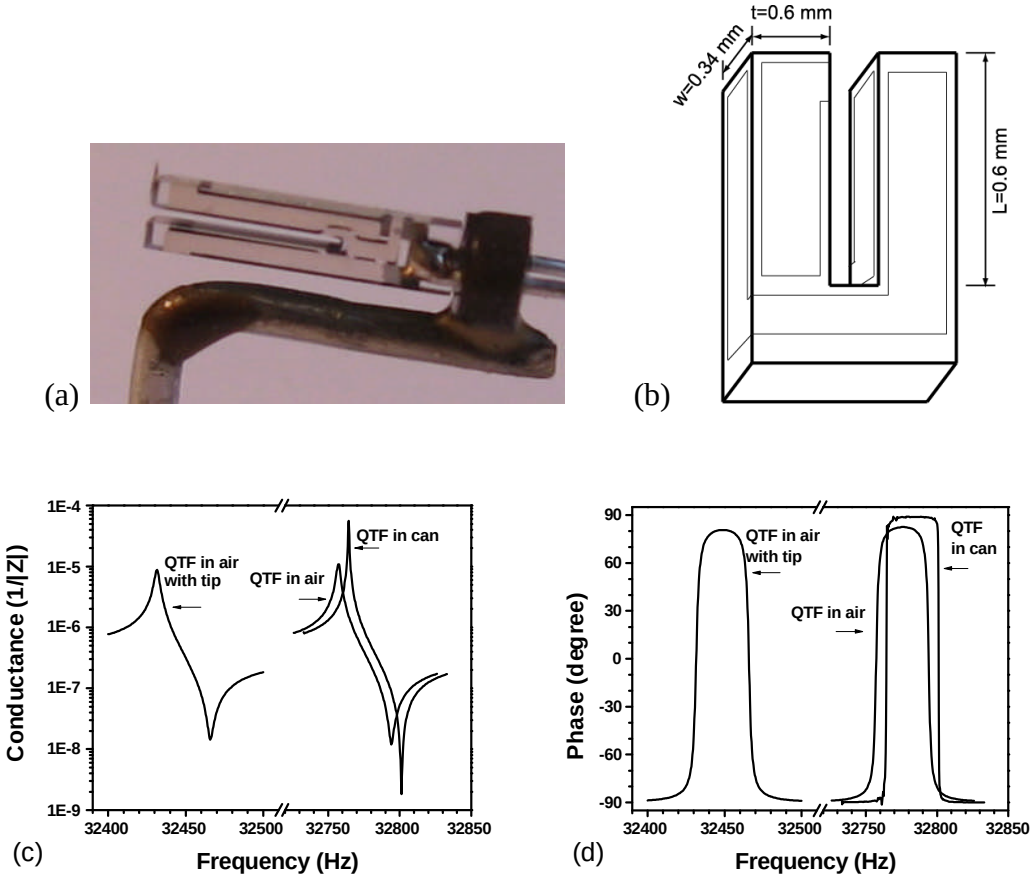

Fig. 3.3 Quartz Tuning Fork impedance. (a) QTF sensor with a tip glued on one prong. (b) Dimensions of QTF ECS-3x8. (c) Conductance of QTF (Inverse of resistance) (d) Phase of QTF.

Once the QTF is connected into the AFM feedback loop, we can use the thermal excitation to calibrate the sensitivity,[59] which is defined to be the ratio of the

measured output signal (in volts) to the QTFs vibration amplitude (in meters). The sensitivity is a figure of merit, since it indicates whether the measured output signal is able to distinguish a small vibration.[60] The output signal, V_{rms}, to be fed into a lock-in amplifier, is obtained by integrating over the resonance frequency $V_{rms}^{2}(df) = \int_{f_0-\delta f/2}^{f_0+\delta f/2} V_{total,rms}^{2}\, df$. The integration is centered at f_0 with a full width of df .We find that $V_{rms}(df)$ saturates quickly as df increases, reflecting the narrowness of the resonance. For example, at 4.2K, V_{rms} reaches 90% of its saturated value (4.563×10^{-6}V) for df =0.184 Hz. The thermal vibration amplitude $\sqrt{\langle x\rangle^2}$ is estimated by equating[61] the thermal energy k_BT to the mechanical energy $k_Q\langle x\rangle^2$, where k_Q is the spring constant, k_B =1.3806503 × 10^{-23} m^2 kg s^{-2} K^{-1} is the Boltzmann constant, and T is the absolute temperature. Given the dimensions, shown in Fig.3.3(b), and the Young's modulus, k_Q is calculated to be 26000N/m by $k_Q = \frac{1}{4}\times Y\times w\times\left(\frac{t}{L}\right)^3$, where Young's modulus $Y = 7.87\times10^{10}\, N/m^2$. And it is a weak function of temperature. We obtain thermal mechanical vibration amplitude of $4.7\text{x}10^{-14}$ m. The sensitivity is therefore determined to be $V_{rms}/\sqrt{\langle x\rangle^2}$ =97μV/pm. Similarly, at 300 K, due to thermal broadening, V_{rms} rises to 90% of its saturation value ($3.5\text{x}10^{-6}$ V) with df=1.25 Hz. The calculated $\sqrt{\langle x\rangle^2}$ at 300 K is $4\text{x}10^{-13}$ m, yielding a sensitivity of 8.75 μV/pm. Cooling the QTF from 300 to 4.2 K increases the sensitivity by a factor of 11. We also can estimate the oscillation amplitude based on the sensitivity we get above. At 300K, the sensitivity is 8.75μV/pm. When the

output signal amplitude is 17.7mVrms (50 mVpp), the QTF oscillation amplitude will be around 2 nm.

3.4 Noise analysis [60]

The QTF does not bring additional signal to the noise spectra when it is off resonance, apparently due to its otherwise large internal impedance. At low frequencies, the noise reflects a $\sim 1/f^{x}$ feature (x>1), inherited from the operational amplifier and the MESFET. In the flatband region, there is amplified input voltage noise, and the gain (defined to be $1/\beta(\omega)$) is determined by the feedback network. At frequencies higher than the flat band, the noise decreases owing to the diminishing gain. To understand the noise spectrum density, Yang et al.[60] followed the standard analysis technique, and arrived at $V_{total,rms}^2(\omega) = \left|\frac{A(\omega)}{1+A(\omega)\beta(\omega)}\right|^2 V_{in,rms}^2(\omega) + 4k_B T R_f$,

Where $A(\omega) = \frac{A_0}{1+\frac{j\omega}{\omega_0}}$ and $\beta(\omega) = \frac{Z_g(\omega)}{Z_g(\omega)+Z_f(\omega)}$.

$V_{in,rms}^2(\omega)$ is the equivalent input noise spectrum density at the gate terminal of the MESFET, $4k_B T R_f$ is Johnson noise of R_f , A_0 is the open loop gain of the operational amplifier. ω_0 is the pole frequency of the operational amplifier. $1/\beta(\omega)$ is the noise voltage gain, $Z_g(\omega)$ is the impedance in front of the gate terminal, $Z_f(\omega)$ is impedance of the feedback resistor. $V_{in,rms}^2(\omega)$ is the sum of the spectral density of two components: (1) the equivalent input voltage noise of the operational amplifier that propagates to the gate, and (2) the drain current noise of the MESFET. A large input capacitance at the gate will likely increase the noise because that reduces $Z_g(\omega)$ and results in a higher noise gain. As of the feedback resistor, large R_f is

preferred. Although its Johnson noise is increased, the transimpedance gain is linearly proportional to R_f, and thus the signal to noise ratio scales up as $\sqrt{R_f}$. Due to the inherent parallel capacitance, the bandwidth is still limited by the time constant $R_f C_f$. Fig. 3.4 shows the noise spectrum measured at OPA602 output. We find that the white noise level, which will determine the signal to noise ratio after the transimpedance amplifier, is determined by the pair of MESFETs.

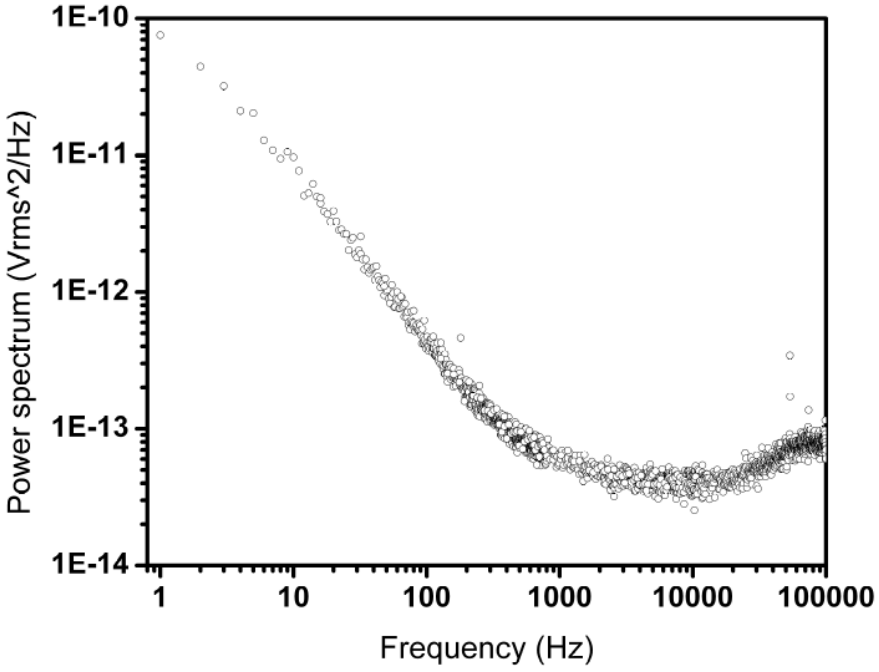

Fig. 3.4 OPA602 output signal noise spectrum measured when feedback loop hasn't been established.

To test the performance of our system, we used etched sharp Pt/Ir tip and scanned the gold film at 300K. We got the AFM images shown in Fig. 3.5. As we can see from Fig. 3.5 (b), the lateral resolution is <10nm and vertical resolution is ~2Å

(a)

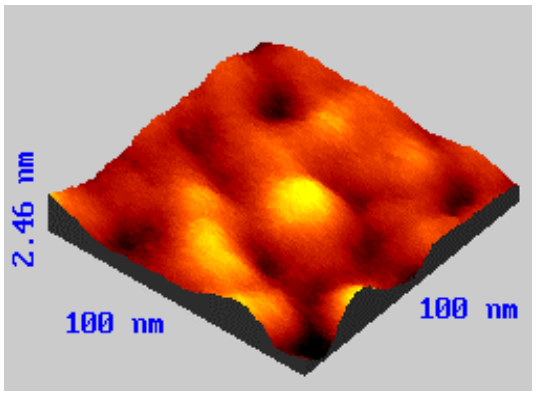

(b)

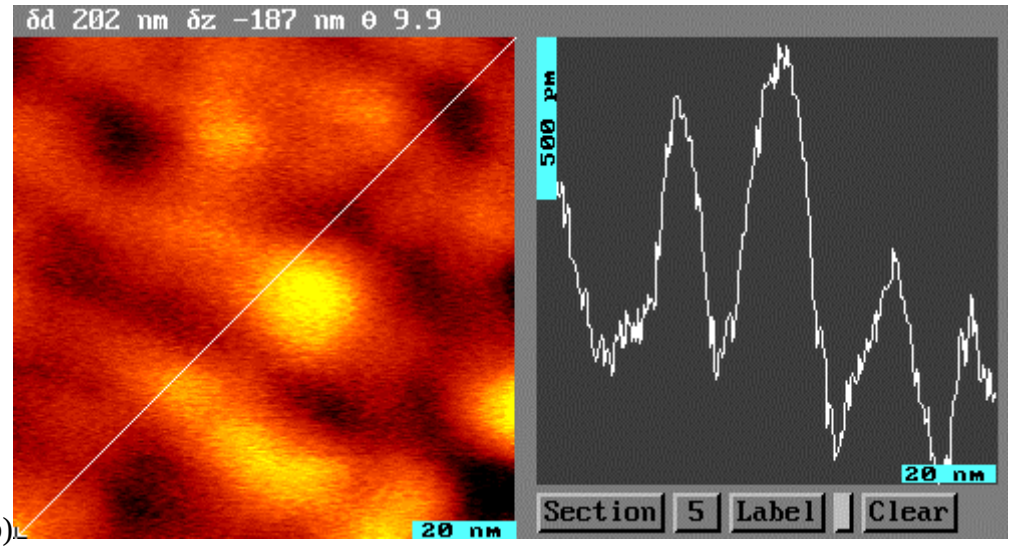

Fig. 3.5 AFM images of gold film scanned at 300K. (a) 3D view of an AFM image of gold film at 300K. (b) Topography of gold film and cross section view along the white line.

Figure 3.6 is one typical approach curve measured at ambient condition. From this approach curve, we can derive that the slope of the imaging signal with respect to z is $\partial \nabla f / \partial z$ =4.8Hz/nm at the set point +2Hz. Using the measured frequency noise in the imaging signal $\delta \Delta f$ =(0.02V/10V)*183.5Hz=0.367Hz. We can estimate the minimum detectable height as δz = 0.367Hz/(4.5Hz/nm) = 0.76Å.

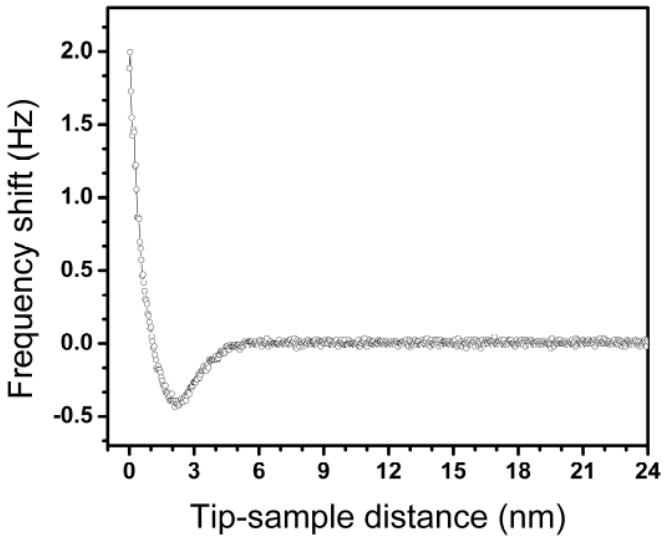

Fig 3.6 One typical approach curve measured at ambient condition. The tip used is electrochemically etched Ni wire, and the sample is 40nm thick gold film on silicon.

Chapter 4 Experiments

4.1 Resonant Interband Tunneling Diode (RITD)

The structure is grown using Molecular Beam Epitaxy (MBE) on n^+ InAs(001) substrate. An n-type doped InAs buffer layer is first deposited. After grown a 10nm undoped InAs spacer layer, AlSb(6nm)/GaSb(5nm)/AlSb(6nm) structure is grown. On the top of the double barrier is 10nm undopled InAs spacer, followed by 10nm n-type doped InAs cap layer.[62] Fig. 4.1 is the energy band diagram of the RITD structure. As we can see in Fig. 4.1, Fermi level is pined above InAs conduction band minimum and also below the valence band maximum of GaSb layer. Therefore the tunneling will occur from InAs conduction band to GaSb valence band through AlSb barrier at close-to-zero bias condition.

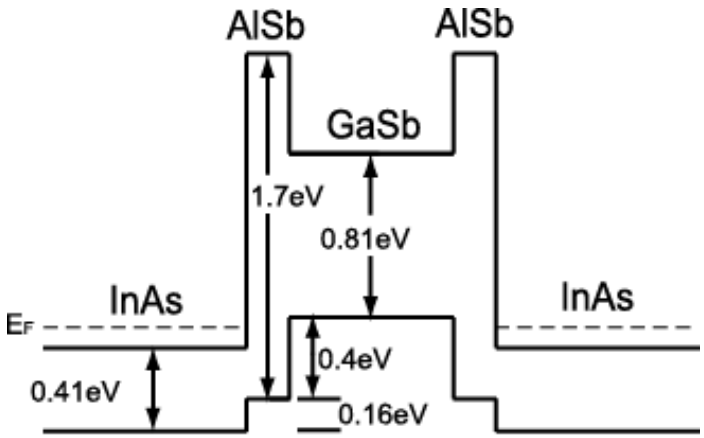

Fig. 4.1 RITD energy band structure

Based on the RITD structure, dots and markers have been fabricated using electron-beam lithography and wet chemical etching techniques developed recently.[63] Two highly selective etching recipes, acetic acid (H_2O_2: H_2O) for InAs and HF: H_2O_2: H_2O for AlSb, will be used. Using electron beam lithography, We first pattern an array of circular holes with different diameters and markers on a bilayer

electron beam resist which is 200 nm poly(methylmethacrylate) (PMMA) on top of 500 nm poly(methylmethacrylate-Co-methacrylic acid) P(MMA/MAA).[64] With metal evaporation and lift-off process, Ti/Au(10nm/30nm) circular disks and markers have been defined as the etching mask for further chemical etching. The disk diameter ranges from 0.2μm to 1.0μm with 0.1μm increment, and the dot sizes range from 0.03μm^2 to 0.8μm^2. After removing the top InAs layers, shown in Fig. 4.2(a), we do current-voltage measurements on those dots. After second etching, shown in Fig. 4.2(b), the double barrier interband resonant tunneling structure has been removed. And then we do current-voltage measurements again.

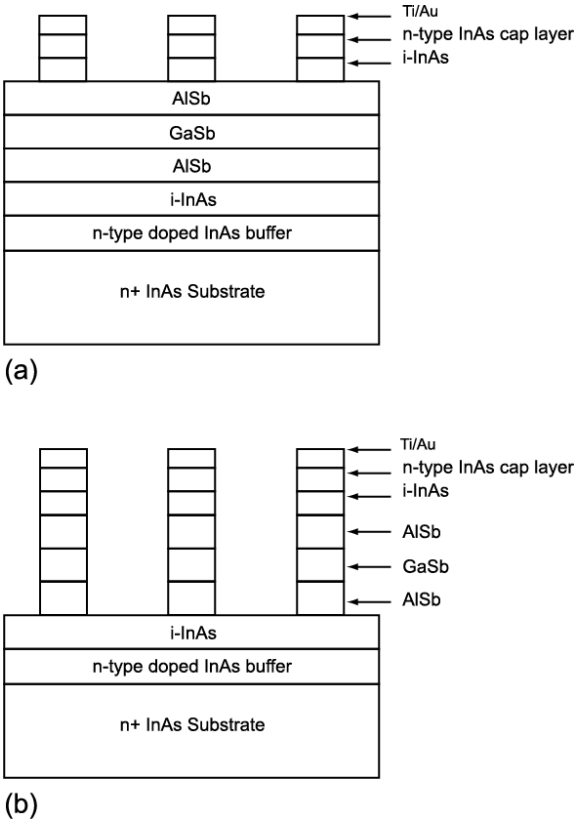

Fig. 4.2 RITD structures. (a) After first etching, top InAs layers are removed. (b) Second etching removes the AlSb/GaSb/AlSb double-barrier interband resonant tunneling structure around the dots

I-V measurements are performed with the homemade AFM system in vacuum (5×10^{-5} Torr) at room temperature first. The AFM is first operated in the topographic mode to locate dot array. The AFM image of dot array is shown in Fig. 4.3(a). Then we identify one dot we want to measure and move the dot to the center of the field by moving coarse x/y stage. Fig. 4.3(b) is the AFM image of one 0.9μm-diam dot which has been moved to the center of the view. Once a particular dot is moved below the tip, we turn off the feedback loop, and the conductive tip can be lowered down step-by-step and physically contact to the dot by external z position modulation. Then we use RHK to record the current through the dot while sweeping the voltage across the desired range.

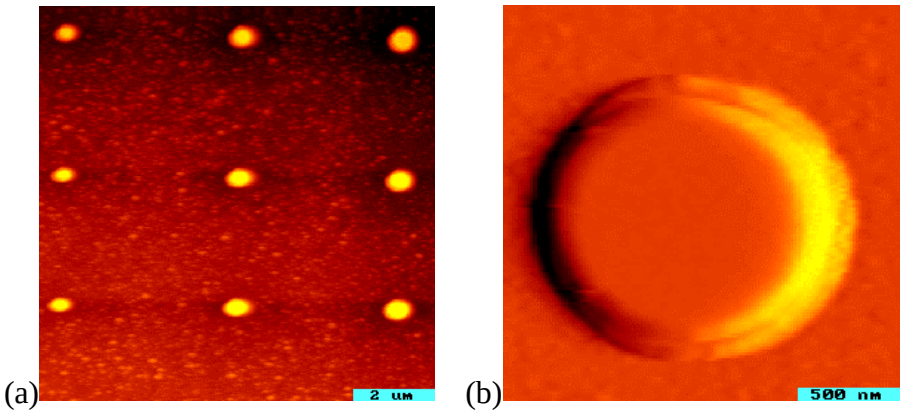

Fig. 4.3 (a) AFM images of AlSb/GaSb quantum dot array measured at room temperature. (b) Similar AFM image of one 0.9μm-diam dot in the center of the field.

In Fig. 4.3(a) the distance between two nearest dots is 4μm. We start our measurement from the smallest dot whose diameter is 0.1 μm. The reason is that after each direct contact current-voltage measurement, the curvature of the tip could be even larger. Once the tip curvature is larger, it will be more difficult to locate the tip exactly on the smallest dot.

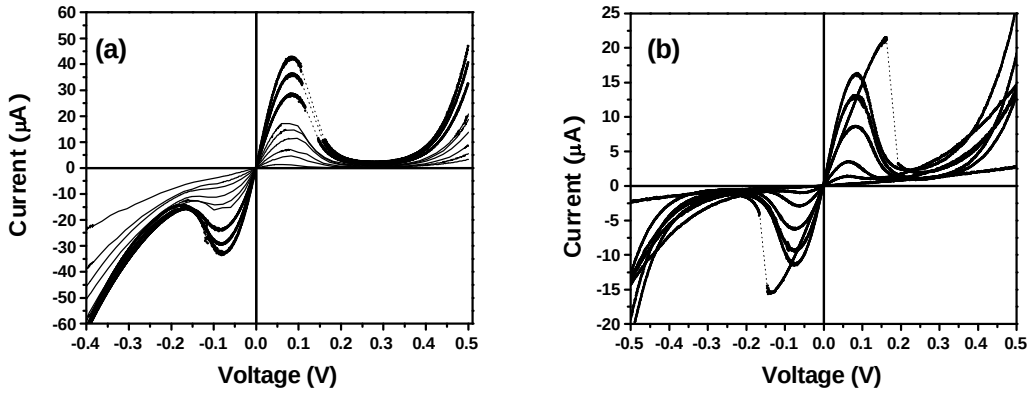

Fig. 4.4 Current-voltage characteristics of A/Sb/GaSb quantum dots measured at room temperature. Dots with larger diameter have larger peak current. (a) I-V curves of dots whose diameters vary from 0.2μm to 1.0μm with an increment of 0.1μm after first etching. (b) I-V characteristics of dots whose diameters vary from 0.4μm to 1.0μm with an increment of 0.1μm after the second etching.

Figure 4.4 Shows the I-V characteristics of a series of diodes with different sizes, where (a) are obtained after the first etching, and (b) are obtained after second etching. Please see Fig.4.2 for the structure details of those dots. The dots with larger diameter show oscillation in the negative differential resistance region, which is represented by dotted line segments. Asymmetry in the measured I-V characteristic has been observed even though there is no intended asymmetry heterostructure grown by MBE. The measured peak/valley voltage is different for positive bias and negative bias, and the peak current densities for positive biases are larger than those for negative biases. These effects may be due to unintentional doping or structural asymmetries in the devices.

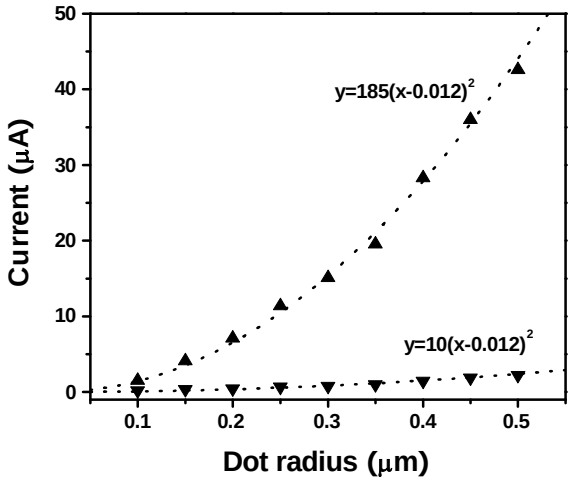

Fig. 4.5 Peak current (up triangle) and valley current (down triangle) as a function of dot radius after the first etching. Dash lines are fitting curves with the shown equations.

Figure 4.5 shows the peak/valley current as a function of the diode radius after the first etching. The area dependence of peak and valley currents has been well modeled by the expression $I = J\pi(r - C)^2$. Where J is the current density, r is the device radius. Peak current density of the diodes is about 5.9kA/cm^2, and valley current density is about 320A/cm^2. The current peak-valley ratio is 18.5. Here C = 0.012 μm, which is effective dot radius reduction due to the lateral extension of the etching undercut. One promising feature of our devices is that their current peak-valley ratio is high as 18.5 even for device with active area as small as 0.03μm^2 and the peak voltage less than 0.1V.

After second chemical etching, the devices show different I-V characteristics. The peak currents decrease, and the valley currents deviate from the relation for device with radius smaller than 0.35μm as shown in Fig. 4.6. The peak current

density is calculated as 5.9kA/cm^2. The valley current density is about 640A/cm^2. The current peak/valley ratio is about 9. The current leakages through the edges of the dots probably result in the high valley current and also reduce the current peak/valley ratio.[65]

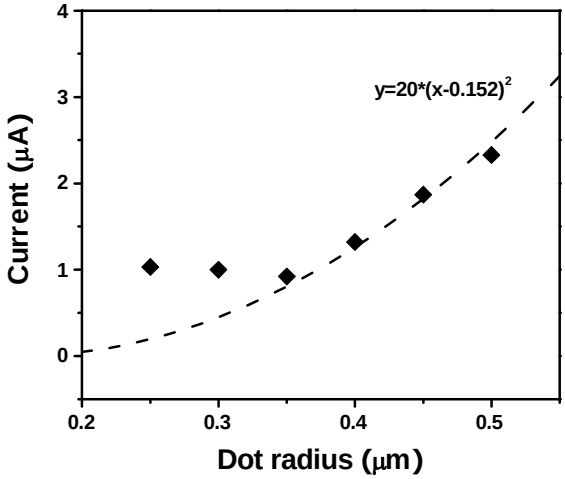

Fig. 4.6 Valley current (diamond) as a function of device radius after second etching. The dash line is a fitting curve with the shown equation.

Figure 4.7 shows the peak current after the first and second etching of the devices as a function of diode radius. As mentioned above the relation can be well modeled by the expression $I = J\pi(r - C)^2$, where C is a constant. C can be etching undercut, which will apply to the two cases, and size reduction due to the depletion, which is the case after the second etching. The difference of C between the two cases is the depletion depth, which is estimated 0.14μm. The equivalent depleted diameter will be 0.3μm, which is consistent with our observation that after the second etching, the diodes (0.2μm and 0.3μm diameter) with diameter smaller than 0.4 μm are pinched off, and the current through those dots is extremely low.

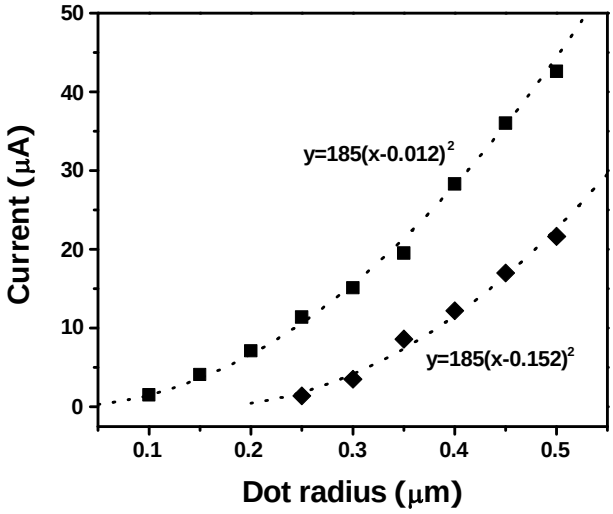

Fig. 4.7 Peak current as a function of dot radius. Squares represent the peak current after the first etching, and diamonds represent the peak current after second etching. Dash lines are fitting curves with the shown equations.

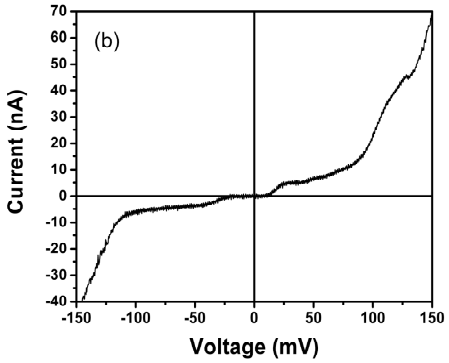

Fig. 4.8 Current-voltage curve of etched 450nm diameter dot measured at 4.2K.

To further prove the quantization effect in the dots, we have measured the current-voltage characteristics for those dots after the second etching, whose surrounding double barrier structures are etched. In fig. 4.8, we can see clear Coulomb blockade and Coulomb staircase on the current-voltage curve for the 450nm diameter dot, while clear NDR current-voltage curve can be seen for both 400nm diameter and 500nm diameter dots. The Coulomb staircase feature reflects the

addition-energy spectrum, i.e., the lowest three additional single electron states are populated near 15mV, 42mV and 90mV, respectively. A qualitatively similar staircase feature is also observed in the negative voltage range while electrons are injected from the tip to substrate.

4.2 EFM

The operating principle of EFM is based on the fact that the potential difference between tip and sample will reduce the resonance frequency of the QTF. Before doing EFM imaging, we do approach curve measurement to see if the complete approach curve can be seen and also make sure the minimum frequency shift value is larger than our set point we want to choose.

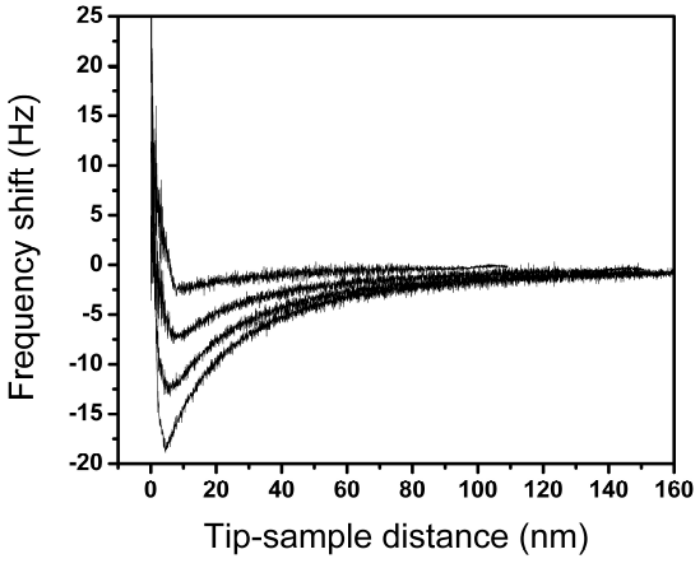

Fig. 4.9 Approach curves with electrostatic force between tip and sample. From the top to bottom, Sample-to-tip biases are +5V, +10V, +12V and +13V.

As we can see in Fig. 4.9, sample-to-tip potential difference dramatically reduces the minimum value of frequency shift. This is because the attractive force between tip and sample reduces the resonance frequency of the quartz tuning fork.

When the tip-to-sample distance is further reduced, the atomic force between tip and sample will be dominant. The repulsive force between the tip and the sample increases the QTF resonance frequency. We also have measured EFM approach curves by switch the sign of tip and sample bias, no difference can be seen because the force between tip and sample is still attractive. After measurement the EFM approached curved shown in Fig. 4.9 we are confident to choose –2.8Hz as our feedback set point if the sample-to-tip potential difference is larger that 5V.

The main operating procedure of reverse mode FM-EFM is very similar to normal mode FM-AFM except that the tip-to-sample potential difference is tunable by change the sample bias and also we choose the set point at the reverse mode region, shown in Fig. 4.10.

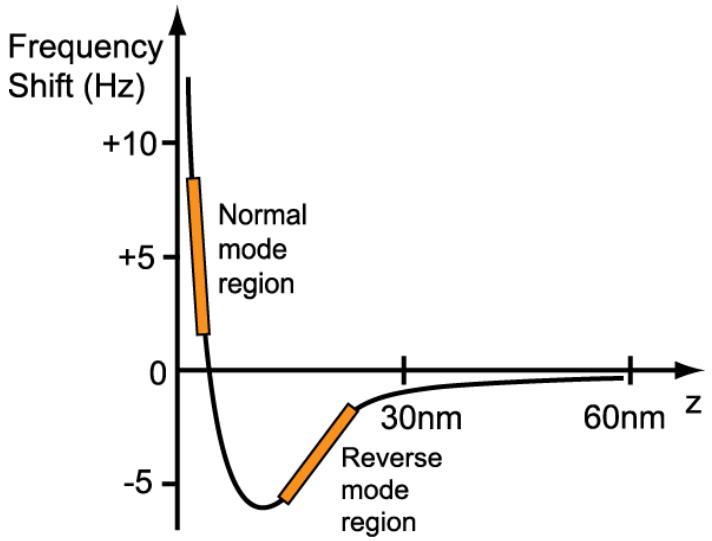

Fig. 4.10 Typical EFM approach curve under 10V sample-to-tip potential difference.

Figure 4.11 shows the system circuit diagram for the EFM measurement. -2.8Hz has been chosen as the feedback set point, and the easyPLL will generate –153mV DC voltage and feeds it to the RHK “input signal”. Once reverse mode is

chosen by setting RHK control unit, “Negative” tip guard must be selected on the easyPLL control panel to make sure the tip would not be damaged easily.

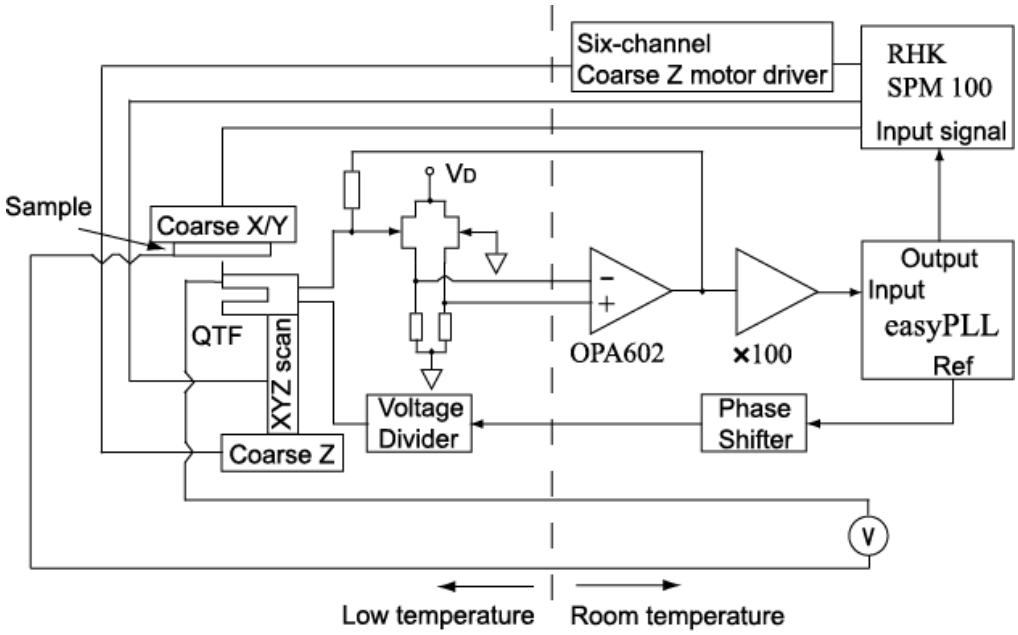

Fig. 4.11 Electrostatic Force Microscope system circuit diagram

Our sample is E-beam lithography patterned conductive stripes on silicon with 500nm spacing. External metal wires are connected to those bonding pads on those conductive stripes, so that we can control the potential on each strip. Usually we do AFM imaging first to find out those conductive stripes. The reason is that the conductive stripes are located in a very small range (90μm×90μm). Once the tip cannot be located right above those stripes, the –2.8Hz set point will never be achieved.

Figure 4.12 is the EFM image we have gotten. The difference between image (a) and image (b) is that the marked strip is biased at +5V for (a) and zero biased for (b). Tip is +10V biased. And all other regions are biased at 0V. From fig.4.12, we can say that the potential difference has been clearly observed.

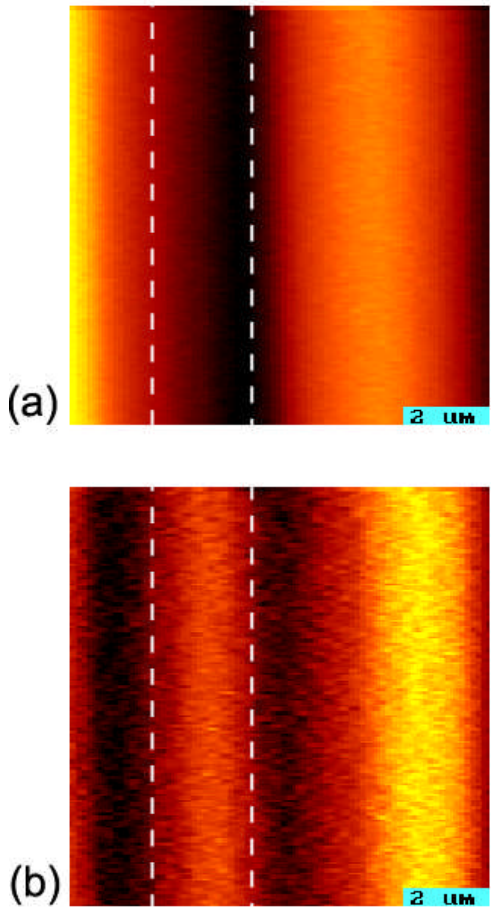

Fig. 4.12 EFM images. The biases on the strip between those two dashed lines are different. The strip is +5V biased in (a) and 0V biased in (b). Tip is +10V biased. And all other strips are 0V biased.

4.3 MFM [66-67]

Figure 4.13 shows the schematics for MFM measurements. First of all, we use schematics (a) to setup the feedback loop, and find out the resonance frequency of the specific QTF with tip. Generally we will choose +2Hz as the feedback set point and run auto approach. After this step, the global feedback loop is established, and the tip will be very close to the sample (~2nm) and the tip to sample distance will be kept at

constant automatically controlled by the feedback loop. We choose appropriate scan parameters to scan AFM image.

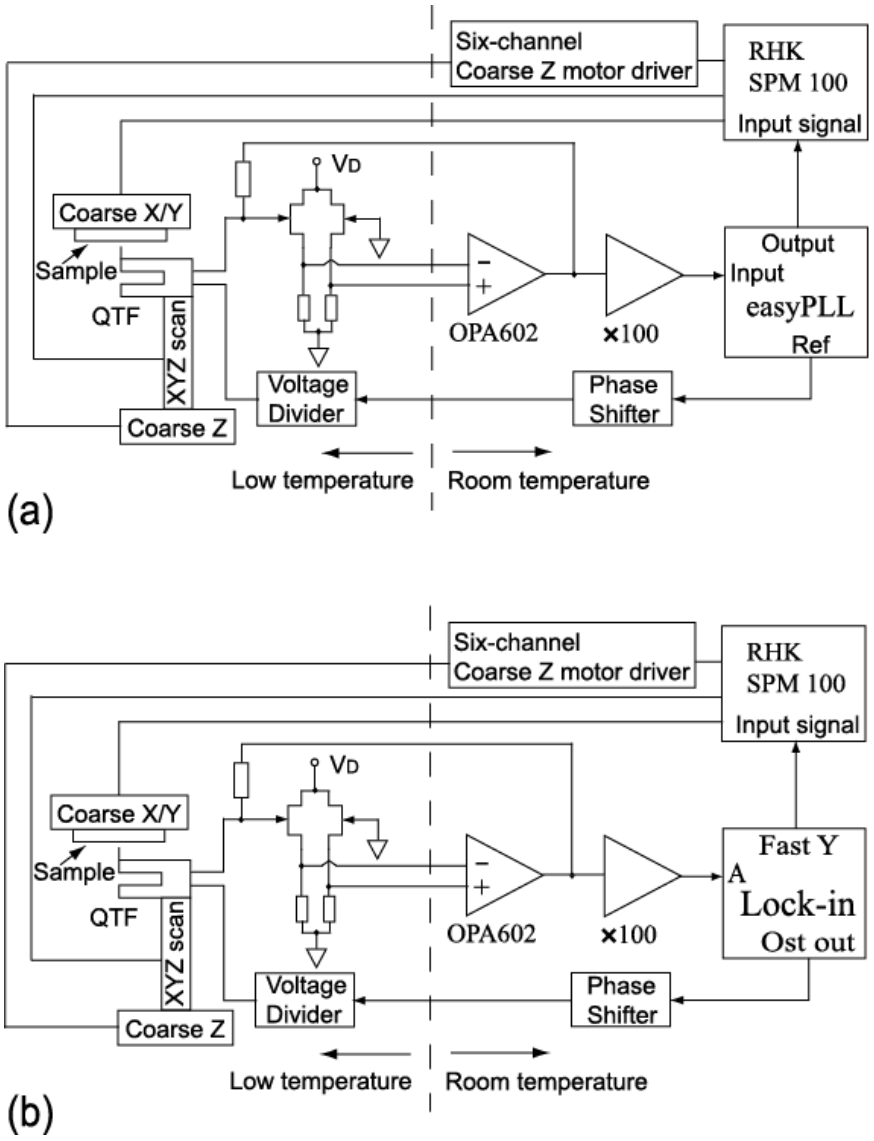

Fig. 4.13 Circuit diagram of MFM measurements

After AFM image scanning, we turn off the feedback loop and retract the tip away from the sample about 50nm. We use the “Bias” on the RHK as the control voltage, which is connected to “Modulation Input Position #1”. The signal applied to the “Modulation Input Position #1” will be amplified by 15.6 and then applied to the Z piezo tube. Based on the conversion ratio of Z piezo tube that is 7.78nm/V, we will

choose the bias voltage –0.39V. Therefore the distance between the tip and sample will be -0.39V*15.6*7.78nm/V= - 47.33nm. Then we change the circuit configuration to schematics (b). The lock-in 7265 will be in the loop instead of easyPLL used in schematics (a). We set the oscillator signal frequency as QTF resonance frequency f_0, choose typical amplitude 5Vrms and select internal reference. We use the "osc out" signal to excite QTF through a 100:1 voltage divider. We feed the output signal from the homemade transimpedance amplifier and x10 voltage amplifier to the lock-in 7265 channel A. This signal will be measured by a lock-in 7265. We can set the phase to be zero by changing phase shift value in the lock-in. Therefore the "Fast Y" signal will be proportional to the phased signal during scanning because Y = amplitude*sinθ ≈ amplitude*θ. We feed Fast Y signal, which is proportional to the phase value, to the input of the RHK and scan MFM image. During MFM scanning, the feedback loop is always off. The QTF force sensor will detect the force gradient change at different locations on the sample during scanning. And the force gradient change will change the resonance frequency of the QTF and its phase of course. Therefore, the force gradient signal will be mapped during x/y plan scanning. Because the tip to sample distance is about 50nm, the atomic force between tip and sample will not be detectable. So only magnetic information will be recorded.

Figure 4.14 are topography and MFM images of Seagate 2.1G hard drive. We can clear see the magnetic domain in the MFM image. The measured bit size is about 250nm and the distance between two tracks is 4.4μm, while the bit size and track distance are 221nm and 4.27μm respectively based on the hard drive specification.

We also can see that the MFM image has no relationship with the topography even though they are the same area.

(a) 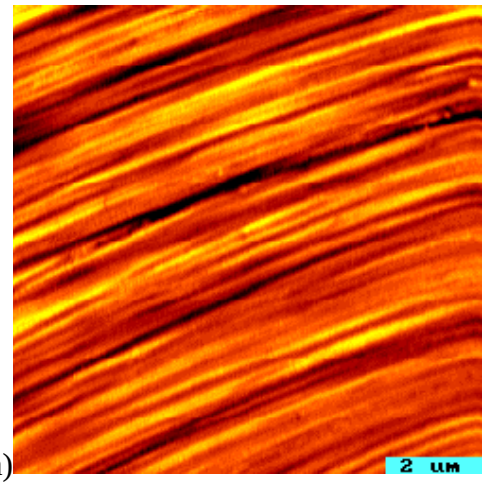

(b) 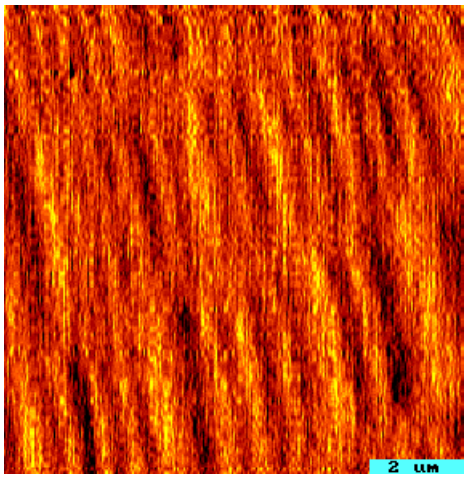

Fig. 4 14 Seagate 2.1G hard drive topography and MFM images. The scan areas for the two images are both 10μmx10μm. (a)Topography. (b) MFM image.

Chapter 5 Conclusion

The design and applications of a cryogenic atomic force microscope for characterization of nanostructures are presented in this thesis. Less than 10nm horizontal and ~ 2Å vertical resolution AFM images has been achieved. We have observed strong Negative Differential Resistance (NDR), Coulomb blockade and Coulomb staircase phenomena in the AlSb/GaSb interband tunneling diodes. This atomic force microscope has also demonstrated EFM and MFM applications. This cryogenic atomic force microscope could be one powerful tool to characterize nanostructure at low temperature.

Appendix A: Tip's equation of motion

We model the cantilever that acts as the tip in the AFM as a spring. Using Hooke's law ($F(z) = -kz$) and Newton's second law ($F = ma$) we have,

$$m\left(\frac{d^2z}{dt^2}\right) = -kz \tag{1}$$

In AFM, damping and driving forces need to be considered. The damping force $F_{damp} = -b(dz/dt)$ and the driving force $F_{drive} = F_0\cos(\omega_d t)$, where b is the damping factor which is related to the quality factor Q by $b = m\omega_0/Q$, and ω_0 is the tip's resonance frequency when there is no driving force applied. Therefore we have $m\frac{d^2z}{dt^2} = -kz - \frac{m\omega_0}{Q}\frac{dz}{dt} + F_0\cos(\omega_d t)$. Change the form of this equation we get

$$m\frac{d^2z}{dt^2} + kz + \frac{m\omega_0}{Q}\frac{dz}{dt} = F_0\cos(\omega_d t) \tag{2}$$

This is the tip's equation of motion, which is the equation of motion of a damped driven harmonic oscillator when there is no tip-sample interaction.

Now, consider the tip-sample interaction term $F_{ts} = -\frac{\partial F}{\partial z}z$, we get

$m\frac{d^2z}{dt^2} = -kz - \frac{m\omega_0}{Q}\frac{dz}{dt} - \frac{\partial F}{\partial z}z + F_0\cos(\omega_d t)$. Again, change the form of the equation, we have

$$m\frac{d^2z}{dt^2} + m\frac{\omega_0}{Q}\frac{dz}{dt} + (k + \frac{\partial F}{\partial z})z = F_0\cos(\omega_d t) \tag{3}$$

Both equation (2) and (3) are non-homogeneous second order differential equations.[1] The solution to both of these equations is the solution to the

corresponding homogenous differential equation plus the particular solution of the original equation.

The solution to the corresponding homogenous equation of equation (3) is

$$z_c(t) = e^{-\beta t}[A_1 \exp(\sqrt{\beta^2 - \omega_0^2}\,t) + A_2 \exp(-\sqrt{\beta^2 - \omega_0^2}\,t)] \tag{4}$$

Where $\beta = \frac{\omega_0}{2Q}$ and $\omega_0^2 = (k + \frac{\partial F}{\partial z})/m$. This equation can be rewritten as

$$z_c(t) = A_t e^{-\beta t}\cos(\omega_t t + \delta_t) \tag{5}$$

Where, A_t and δ_t are adjusted to fit the boundary conditions.

The particular solution of equation (3) is

$$z_p(t) = \frac{F_0/m}{\sqrt{(\omega_0^2 - {\omega_d}^2)^2 + (\frac{\omega_0\omega_d}{Q})^2}}\cos(\omega_d t + \delta') = {A_0}'\cos(\omega_d t + \delta') \tag{6}$$

Where $\delta = \tan^{-1}(\frac{\omega_0\omega_d}{Q}({\omega_0}^2 - {\omega_d}^2))$.

It is convenient to identify $z_c(t)$ as the transient solution, which is dependent on the initial conditions, and $z_p(t)$ as the steady state solution, which is dependent only upon the driving force. Therefore the general solution of the tip motion equation will be:

$$z(t) = z_p(t) + z_c(t) = A_0'\cos(\omega_d t + \delta') + A_t e^{-\beta t}\cos(\omega_t t + \delta_t) \tag{7}$$

Where ${A_0}'$ and δ' are the new steady state amplitude and phase, A_t and δ_t are adjusted to fit the boundary conditions. In the case of zero tip-sample interactions, both $z_c(0) = 0$ and $\frac{dz}{dt}(0) = 0$, which implies that $A_t = 0$. The solution of the tip equation of motion in this case is simply the particular solution $z_p(t)$.

Rewrite the solution (7) in the form of $z(t) = A(t)\cos(\omega_d t + \delta(t))$, we have

$$A^2(t) = A_0^{'2} + A_t^2 e^{-\omega_0' t/Q} + 2A_0' A_t e^{-\omega_0' t/2Q}\cos[(\omega_t - \omega_d)t + (\delta_t - \delta')] \qquad (8)$$

Now it becomes apparent that the measured amplitude has three components: the new steady-state term, a transient decay term and a transient beat term. Only after a time of $\tau = 1/\beta = 2Q/\omega_0'$ will the transient term disappear and the system will return to a steady state. That is, only after a time τ, may we measure the new amplitude of the cantilever vibration.

Therefore high-Q values offer high sensitivity but slow response. For one example, for a high-Q cantilever in vacuum Q=50000 and a typical resonant frequency of 50kHz, the maximum available bandwidth is only 0.5Hz, which is unusable for most applications. Because of these restrictions, it's not useful to try to increase sensitivity by raising the Q to such high values. Slope detection is unsuitable for most vacuum applications.

While in the FM detection system, a high-Q cantilever vibrating on resonance serves as the frequency-deterring components of an oscillator. Changes in the force gradient $\partial F/\partial z$ cause instantaneous changes in the oscillator frequency which will be detected by a FM demodulator. Therefore fast scan speed is expected by using the FM method.

Reference:

[1]. Farlow, Stanley, An introduction to Differential Equations and their Applications, Ch3, pages 141-186. © 1994 McGraw Hill Inc., New York.

[2]. T.R.Albrecht, P.Grutter, H.Horne, and D. Rugar, J. Appl. Phys. 69, 668(1991).

Appendix B: Circuit diagrams of coarse z motor driving boards

(a). Small signal board

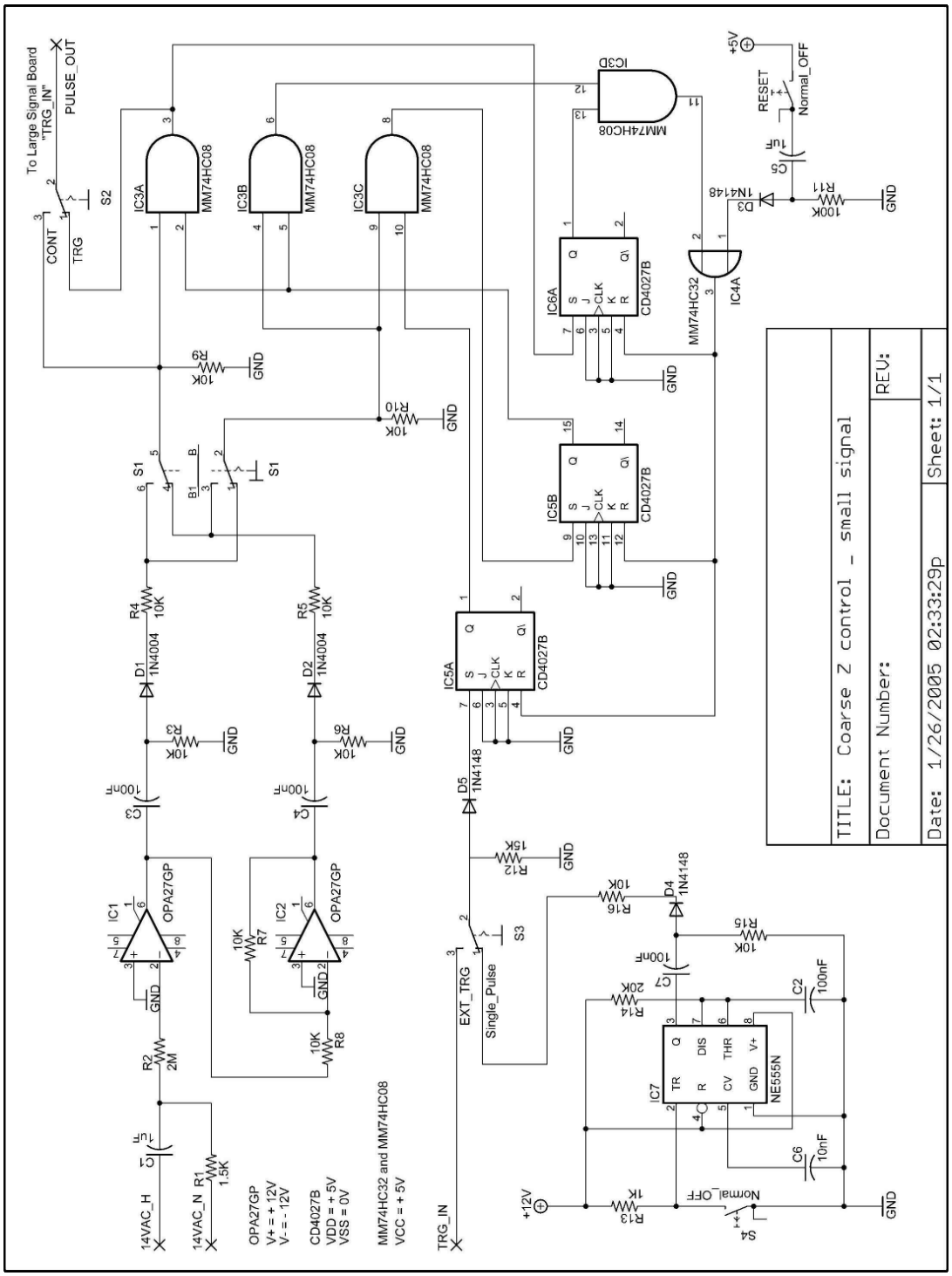

(b). Large signal board

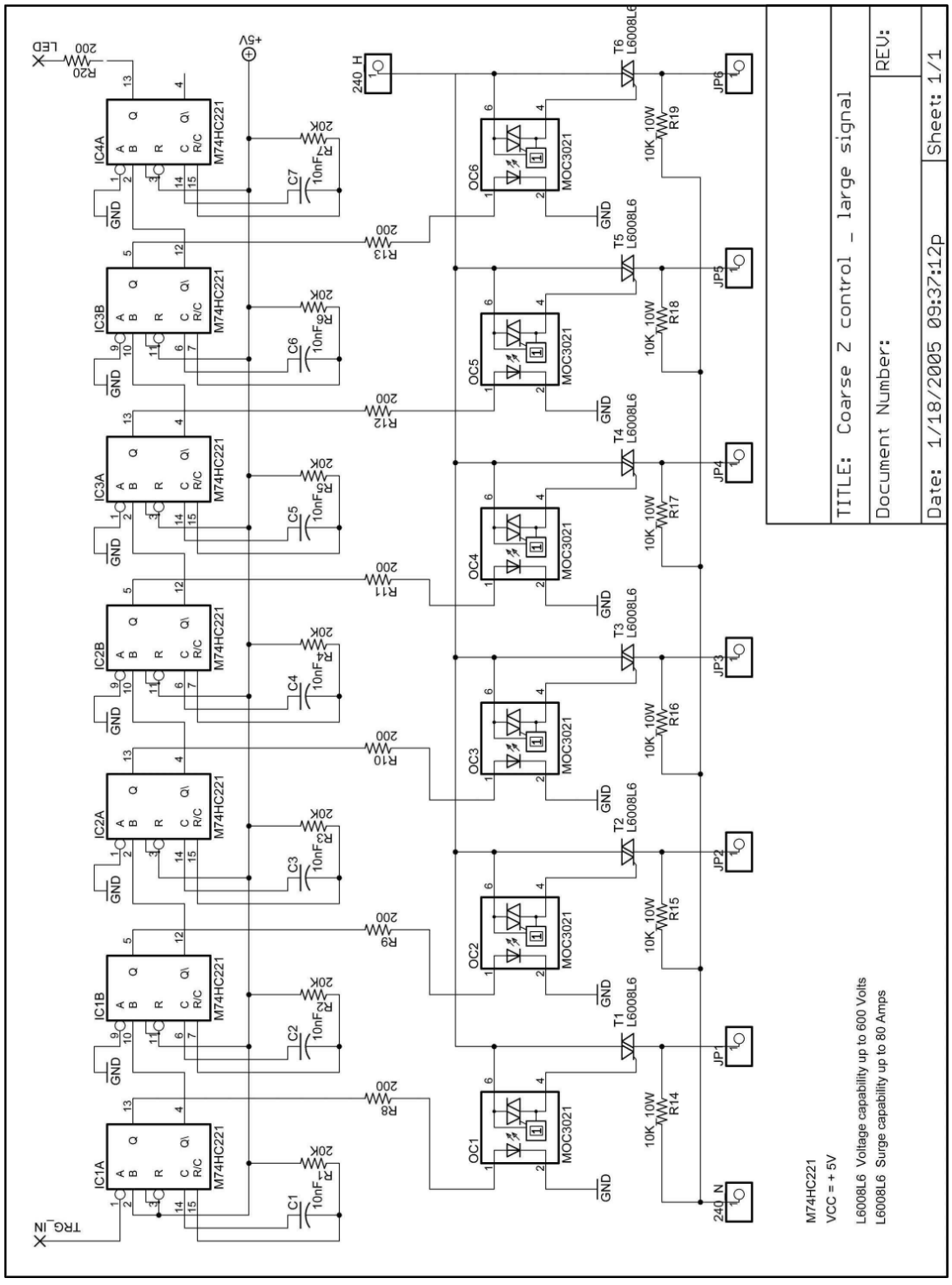

REFERENCE

1. G.Binnig, H. Rohrer, C. Gerber, and E. Weibel, Phys. Rev. Lett. 49, 57(1982).
2. G.Binnig, Rohrer, Gerber and Weibel, Phys. Rev. Lett. 50, 120(1983).
3. W.J.Kaiser and L.D.Bell, Phys. Rev. Lett. 60, 1406(1998).
4. S.A.Elrod, A.Lozanne, and C.F.Quate, Appl. Phys. Lett. 45, 1240(1984).
5. F.J.Giessibl, Rev. Mod. Phys. 75, 949(2003).
6. U.Hartmann, J. Appl. Phys. 64, 1561 (1988).
7. G.Binnig, and H. Rohrer, Rev. Mod. Phys. 59, 615(1987).
8. G.Binnig, and H. Rohrer, Rev. Mod. Phys. 71, S324(1999).
9. H.Güntherodt, and R.Wiesendanger, Eds. Scanning Tunneling Microscopy I-III, Springer, Berlin, 1991.
10. C.J.Chen, Introduction to Scanning Tunneling Microscopy, Oxford University Press, New York, 1993.
11. J.A.Stroscio, and W.J.Kaiser, Eds. Scanning Tunneling Microscopy, 2nd ed. Academic, Boston, 1994.
12. R.Wiesendanger, Scanning Probe Microscopy and spectroscopy: Methods and Applications, Cambridge University Press, Cambridge, UK, 1994.
13. R.Wiesendanger, Scanning Probe Microscopy: Analytical Methods, Springer, Berlin, 1998.
14. U.Dürig, J.K.Gimzewski, and D.W.Pohl. Phys. Rev. Lett. 57, 2403(1986).
15. G.Binnig, “Atomic Force Microscope and Method for Imaging Surfaces with Atomic Resolution”, US Patent No. 4,724,318, (1986).
16. D.Courjon, C.Bainier, and M.Spajer, J. Vac. Sci. Technol. B 10, 2436 (1992).

17. F.Ohnesorge, and G.Binnig, Science 260, 1451(1993).

18. F.J.Giessibl, Science 267, 68(1995).

19. T.R.Albrecht, P.Grutter, H.K.Horne and D.Rugar, J. Appl. Phys. 69, 668(1991).

20. U.Dürig, O.Züger and A.Stalder, J. Appl. Phys. 72, 1778(1992).

21. J.J.Sáenz, N.García, and J.C.Slonczewski, Appl. Phys. Lett. 53, 1449 (1988).

22. A.Wadas and P.Grütter, Phys. Rev. B 39, 12013 (1989).

23. N.Burnham, and R.J.Colton, J. Vac. Sci. Techol. A 7, 2906(1989).

24. F.J.Giessib, Phys. Rev. B 56, 16010(1997).

25. D.Baselt and J.Baldeschwieler, J. Vac. Sci. Technol. B10, 2316(1992).

26. H.Hölscher, A.Schwarz, W.Allers, U.D.Schwarz and R.Wiesendanger, Phys. Rev. B 61, 12678(2000).

27. F. J. Giessibl, Appl. Phys. Lett. 78, 123(2001).

28. F. J. Giessib, and H. Bielefeldt, S. Hembacher, and J. Mannhart, Phys. Rev. B 61, 9968(2000).

29. U. Ch. Fischer and D. W. Pohl, Phys. Rev. Lett. 62, 458 (1989).

30. F. Ohnesorg, and G. Binnig, Science 260, 1451(1993).

31. R.Chatterjee, G.A.Hallock, and M.L.Gartman, Rev. Sci. Instrum. 66, 457(1995).

32. F. J. Giessibl, Phys. Rev. B 45, 13815(1992).

33. Y. Marin, C. Williams, and H. Wickramasinghe, J. Appl. Phys. 61, 4723(1987).

34. T.R.Albrecht, P.Grutter, H.Horne, and D.Rugar, J. Appl. Phys. 69, 668(1991).

35. F.J.Giessibl, Jpn. J. Appl. Phys. 33, 3726(1994).

36. F.J.Giessibl, and B.M.Trafas, Rev. Sci. Instrum. 65, 1923(1994).

37. Y.Martin, C.Williams, and H.Wickramasinghe, J. Appl. Phys. 61, 4723(1987).

38. D.Smith, Rev. Sci. Instrum. 66, 3191(1995).

39. F.J.Giessibl, in Noncontact Atomic Force Microscopy, edited by S.Morita, R.Wiesendanger, and E.Meyer (Spinger, Berlin), Chap.2, 11-46(2002).

40. U.Dürig, H.P.Steinauer, and N.Blanc, J. Appl. Phys. 82, 3641 (1997).

41. F.J.Giessibl, H. Bielefeldt, S.Hembacher, and J.Mannhart, Appl. Surf. Sci. 140, 352(1999).

42. D.Rugar and P.Hansma, Phys. Today 43, 23(1990).

43. Cristian Staii, Nicholas J. Pinto, and Alan T. Johnson, Jr. AIP Conf. Proc. 723, 129 (2004).

44. S.Akamine, R.C.Barrett, and C.F.Quate, Appl. Phys. Lett. 57, 316(1990).

45. O.Wolter, T. Bayer, and J. Greschner, J. Vac. Sci. Technol. B 9, 1353(1991).

46. P.Güethner, U.Fischer, and K.Dransfeld, Appl. Phys. B: Laser Opt.48, 89(1989).

47. K.Karrai, and R.D.Grober, Appl. Phys. Lett. 66, 1842(1995).

48. Dexter Magnetic Technologies, 48460 Kato Rd., Fremont, CA 94538.

49. O.Pietzsch, A.Kubetzka, D.Haude, M.Bode, and R.Wiesendanger, Rev. Sci. Instrum. 71, 424(2000).

50. H.Murakami, T.Ogami, Y.Qi, K.Sakai and T.Ito, Physica B 284, 2063(2000).

51. J.W.Lyding S.Skala, J.S.Hubacek, R.Brockenbrough, and G.Gammie, Rev.Sci.Instrum. 59, 1897(1988).

52. J.W.G.Wildöer, A.J.Avan Roy, H.van Kempen, and C.J.P.M.Harmans, Rev.Sci.Instrum. 65, 2849(1994).

53. Ol.Pietzsch, A.Kubetzka, D.Haude, M.Bode, and R.Wiesendanger, Rev. Sci.Instrum. 71, 424(2000).

54. S.H.Pan, International Patent Publication Number WO 93/19494 (International Bureau, World Intellectual Property Organization), 30 September 1993.

55. S.H.Pan, E.W.Hudson, and J.C.Davis, Rev. Sci. Instrum. 70, 1459(1999).

56. J.Lindahl, T.Ktakanen, and L.Montelius. J.Vac.Sci. Technol. B 16, 3077(1998).

57. D.Rugar, et al. J.Appl.Phys. 68, 1169(1990).

58. C.L.Wyatt, D.J.Baker, and D.G.Frodsham, Infrared Phys. 14, 165 (1974).

59. F.J.Giessibl, Appl. Phys. Lett. 73, 3956 (1998).

60. C.H.Yang, T.H.Chang, M.J.Yang and M.J.Moore, Rev. Sci. Instrum. 73, 2713(2002)

61. F.J.Giessibl, Appl. Phys. Lett. 76, 1470 (2000).

62. M.J.Yang, W.J.Moore, B.R.Bennett, B.V.Shanabrook, J.O.Cross, W.W.Bewly, C.L.Felix, I.Vurgaftman, and J.R.Meyer, J. Appl. Phys. 86, 1796 (1999).

63. M.J.Yang, K.A.Cheng, C.H.Yang, and J.C.Culbertson, Appl. Phys. Lett. 80, 1201(2002).

64. T.H.Chang, C.H.Yang, M.J.Yang, and J.B.Dottelis, Rev. Sci. Instrum. 72, 2989(2001).

65. Patrick Fay, Jiang Lu, Yanyang Xu, Gary H. Bernstein, David H. Chow, and Joel N. Schulman, IEEE Trans. Electron Devices 49, 19(2002).

66. M.Todorovic and S.Schultz , J. Appl. Phys. 83, 6229 (1998).

67. S.Rozhok and V.Chandrasekhar, Solid State Communications 121, 683(2002).